


Article

Design and Analysis of the Mechanical Structure of a Robot System for Cabin Docking

Ronghua Liu ^{1,2} and Feng Pan ^{1,*} ¹ School of Automation, Beijing Institute of Technology, Beijing 100081, China; ronghua5416@163.com² Jiangsu Automation Research Institute, Lianyungang 222061, China

* Correspondence: panfeng@bit.edu.cn

Abstract: Aiming at the disadvantages of traditional manual docking, such as low assembly efficiency and large positioning error, a six-DOF dual-arm robot system for module docking is designed. Firstly, according to the operation tasks of the cabin docking robot, its functional requirements and key indicators are determined, the overall scheme of the robot is designed, and the composition and working principle of the robot joints are introduced in detail. Secondly, a strength analysis of the core components of the docking robot is carried out by finite element analysis software to ensure its load capacity. Based on the kinematics model of the robot, the working space of the robot mechanism is simulated and analyzed. Finally, the experimental platform of the docking robot is built, and the working space, repeated positioning accuracy, and motion control accuracy of the docking robot mechanism are verified through experiments, which meet the design requirements.

Keywords: cabin docking; robot design; strength analysis; work space



Citation: Liu, R.; Pan, F. Design and Analysis of the Mechanical Structure of a Robot System for Cabin Docking. *Actuators* **2024**, *13*, 206. <https://doi.org/10.3390/act13060206>

Academic Editor: Ioan Doroftei

Received: 19 April 2024

Revised: 23 May 2024

Accepted: 26 May 2024

Published: 30 May 2024



Copyright: © 2024 by the authors. Licensee MDPI, Basel, Switzerland. This article is an open access article distributed under the terms and conditions of the Creative Commons Attribution (CC BY) license (<https://creativecommons.org/licenses/by/4.0/>).

1. Introduction

Most aerospace products such as aircraft and rockets are composed of compartments with different structural characteristics. The assembly, testing, and testing process of aerospace products involve complex operations of module docking. At present, in the field of cabin assembly in China, manufacturers generally adopt the traditional assembly mode of “manual as the main, mechanical as the auxiliary”. In this mode, the cabin components to be docked are manually hoisted to auxiliary tools, and the operator estimates the cabin attitude through eye observation. There are some problems such as low docking efficiency, poor docking quality, and unquantifiable docking accuracy. At the same time, when the diameter of the cabin increases to a certain level, the labor intensity increases sharply and the production efficiency decreases sharply. The traditional assembly mode can no longer meet the actual needs of manufacturing enterprises, so it is imperative to improve the automation level of cabin docking.

Regarding the cabin docking robot system, its level of development in foreign countries is relatively mature. Cabin docking mainly includes Three-coordinate POGO column assembly, Stewart platform assembly, Vertical assembly, Horizontal docking assembly, and other forms as follows:

- (1) Three-coordinate POGO column assembly: The three-coordinate POGO column structure is used to adjust the position and pose of the workpiece [1–3]. The POGO column is an adjustable support system with three orthogonal translation degrees of freedom, which is composed of three mutually orthogonal translation units, and can adjust the supported parts in space with high precision. Aiming at the aircraft wing assembly problem, a six-DOF attitude docking system based on a three-DOF POGO column was proposed [4]. Each positioner is connected to the wing by a hemispherical end effector. The positioner and the wing mechanism form a three-PPPS (P is a moving joint, S is a spherical joint) redundant drive variable mechanism. Assembly by the

three-coordinate POGO column makes the production line have high flexibility. However, this assembly method has certain limitations; for example, the distributed POGO column is redundant in motion control, which will bring high difficulty and economic cost to the control.

- (2) Stewart platform assembly: The Stewart platform is used to adjust the position and pose of the workpiece. A Stewart platform refers to a symmetrical parallel mechanism with six degrees of freedom [5,6]. Based on the six-SPS parallel mechanism, which is used to adjust the attitude of the module [7], a force sensor is integrated in each sliver chain of the parallel mechanism to achieve flexible docking control of the module through force feedback, so as to reduce the risk of damaged parts. Compared with distributed POGO columns, the Stewart platform is more compact and easier to control. However, this assembly method has certain limitations for the assembly of cabin parts with different diameters and lengths, and it is not suitable for continuous production in the engineering environment.
- (3) Vertical assembly method: The components of the cabin are assembled vertically by means of lifting assembly. In the automatic docking of a satellite, a six-SPS parallel mechanism is used as the docking equipment to support the mobile module, and the mechanism can dock the mobile module with the suspended fixed module by adjusting its posture in the vertical direction [8]. However, the vertical assembly method requires enough space to be utilized in the vertical direction of the workshop, allowing multiple compartments to be placed vertically, which is not conducive to popularization and application in the general assembly workshop. At the same time, with an increase in the weight and size of the cabin, the vertical assembly method will become difficult to implement because of the difficulty of operation, high-risk factor, and increase in vertical assembly control.
- (4) Horizontal docking method: By lifting or AGV transfer, the cabin components are transferred to the attitude adjustment mechanism of the assembly workstation. The attitude adjustment mechanism can move horizontally along the guide rail to complete the assembly and docking of the multi-stage cabins. Aiming at the docking problem of a certain type of rocket module, the automatic docking platform of the rocket module was built by the Shenyang Institute of Automation [9]. The six-DOF pose adjustment mechanism loaded with ring tooling is used as the pose adjustment platform of the docking module, and the transfer drive and the docking drive of the module are designed in an integrated way. Aiming to address the high precision and automation requirements of spacecraft module docking assembly, the Beijing Institute of Satellite Environmental Engineering proposed large module horizontal docking assembly technology based on automation means [10] and designed the module horizontal docking system structure.

Considering the advantages and disadvantages of the three-dimensional POGO column assembly method, Stewart platform assembly method, lifting vertical assembly method, and horizontal docking assembly method, a six-degree-of-freedom (DOF) cabin docking dual-arm robot system is designed, which has the characteristics of a large load, high flexibility, high precision, quick replacement, and so on. Based on the analysis of the functional requirements and key indexes of the robot system, the technical indexes of the development of the docking dual-arm robot system in the cabin are determined. The system composition and working principle of each joint in the module docking robot are studied in detail, and the strength of each joint core component is analyzed by software. Based on the kinematics model of the robot mechanism, the working space of the robot mechanism is simulated and analyzed. The working space, repeated positioning accuracy, and motion accuracy of the docking robot mechanism are verified by prototype testing.

This paper is organized as follows: Section 2 analyzes the functional requirements and key indicators of the module docking robot. Section 3 introduces the overall scheme of the docking robot system, the composition of each joint mechanism, and the strength analysis results. In Section 4, the kinematic model of the docking robot is established, and the

kinematic simulation is carried out. Section 5 verifies the technical indicators of the docking robot in the module through the prototype. The results are summarized in Section 6.

2. Functional Requirements and Key Indicators of the Module Docking Robot

2.1. Functional Requirements of the Cabin Docking Robot

The main task of the module docking robot system is to realize the automatic attitude adjustment function of a large heavy-duty cabin by designing a six-degree-of-freedom robot mechanism and to complete the automatic docking function of multiple cabin workpieces with the aid of the visual measurement system. The specific functions include the following:

- (1) Carrying a large load and large sized workpieces, and carrying weight not less than 500 kg;
- (2) High precision, reliable and stable motion function;
- (3) A certain product compatibility function that adapt to the compatibility function of different loads within a certain specification range.

2.2. Technical Indicators

In order to accomplish the above tasks, the docking robot has specific requirements for load capacity, working space, moving speed, and so on, as follows:

- (1) Load capacity: including the motion accuracy of the robot platform, the degree of freedom of the robot, the load capacity of the robot, etc. These indicators determine the ability of the robot to perform the final task;
- (2) Working space: the robot must have the working range required for the assembly of cabin workpieces;
- (3) Motion speed: when the docking robot performs the assembly task, the docking robot is required to operate quickly and work efficiently.

The technical indicators of the designed cabin docking robot are shown in Table 1.

Table 1. Main technical indicators of the docking robot system.

Item	Specific Item	Value
Load capacity	DOF	6
	Rated load	500 kg
	Repeated positioning accuracy	± 0.05 mm
	Maximum load	1000 kg
Work space	Circumference roll range	$\pm 15^\circ$
	Axial travel range	± 600 mm
	Vertical lift travel range	± 50 mm
	Radial travel range	± 50 mm
Speed	Circular rolling speed range	0~6.8°/s
	Axial movement speed range	0~400 mm/s
	Vertical lifting speed range	0~4.5 mm/s
	Radial movement speed range	0~25 mm/s
Acceleration	Acceleration range of circular roll	0~240°/s ²
	Acceleration range of axial movement	0~100 mm/s ²
	Acceleration range of vertical lift	0~100 mm/s ²
	Acceleration range of radial motion	0~100 mm/s ²

3. Mechanical Design and Strength Analysis of the Cabin Docking Robot System

3.1. Overall Scheme of the Cabin Docking Robot System

In order to meet the technical indicators in Table 1, a cylindrical cabin workpiece is taken as an example to design a cabin docking robot. The cabin docking robot is mainly composed of a left robotic arm, a right robotic arm, a base, and a control system. The three-dimensional model of the docking robot designed by NX2023 software is shown in Figure 1.

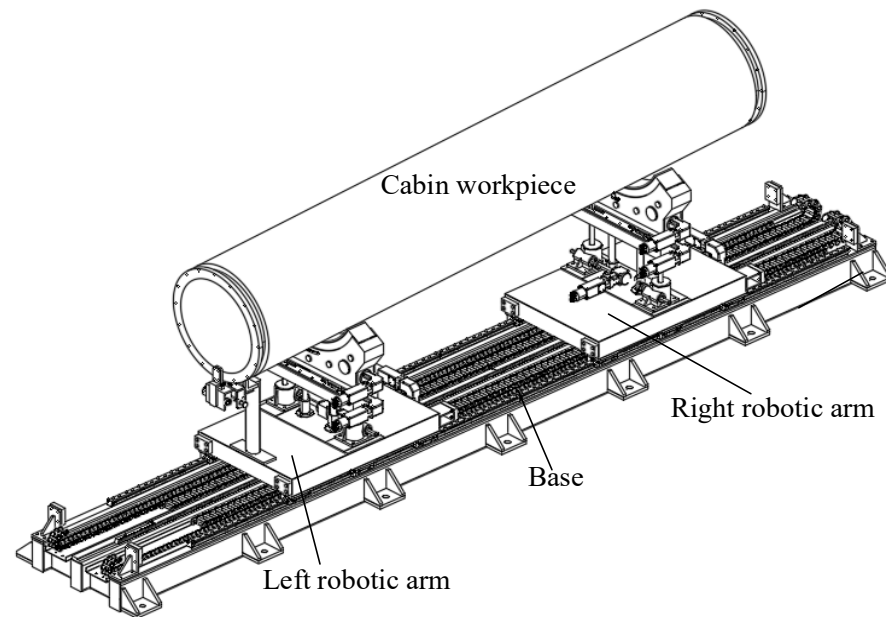


Figure 1. Composition and working diagram of the robot system for cabin docking.

In Figure 1, the docking robot is composed of a left robotic arm, a right robotic arm, and a base. The left robot arm and the right robot arm are connected to the base rail through a slider and move axially through a rack and pinion drive. The left robotic arm and the right robotic arm have the same structure, and each robotic arm includes four joints as follows: axial moving joint, vertical lifting joint, radial moving joint, and circular rolling joint. The composition of a single robotic arm is shown in Figure 2.

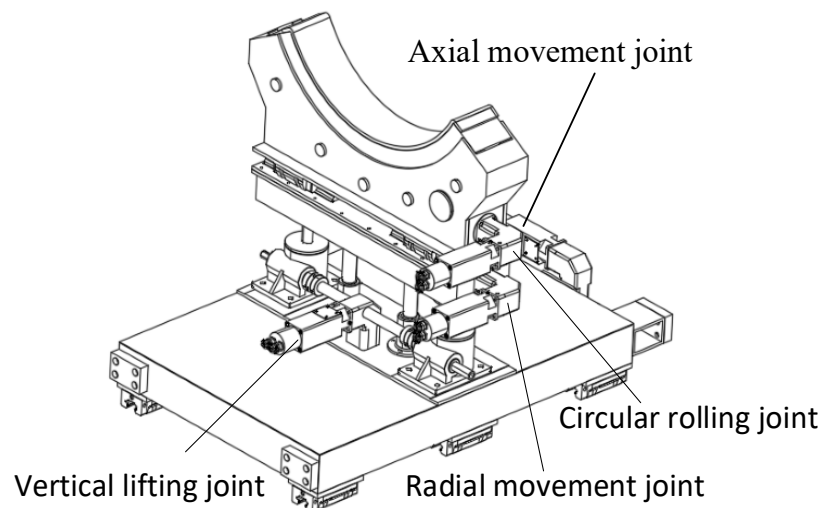


Figure 2. Diagram of a single robotic arm.

As shown in Figure 2, the width of a single mechanical arm is 820 mm, the length is 1200 mm, and the center of the circular rolling joint is 1100 mm above the ground. The docking robot can complete the adjustment of six degrees of freedom (pitch, yaw, roll, radial, lifting, and axial) of the workpiece in the whole cabin. The axial moving joint is driven by the servo motor to achieve axial horizontal action, the radial moving joint is driven by the servo motor to achieve horizontal action in the diameter direction of the screw structure, the vertical lifting joint is driven by the servo motor to achieve the height lifting as the spiral lift, and the circular rolling joint is driven by the servo motor to achieve the circular rotation action.

3.2. Joint Design of the Docking Robot

3.2.1. Axial Movement Joint

The axial movement joint mainly consists of a structural frame, drive gear, servo motor and reducer, slide block, bottom structural frame, and other parts. The servo motor and reducer drive the gear to rotate and then drive the mechanical arm to move the axis on the guide rail of the base, as shown in Figure 3.

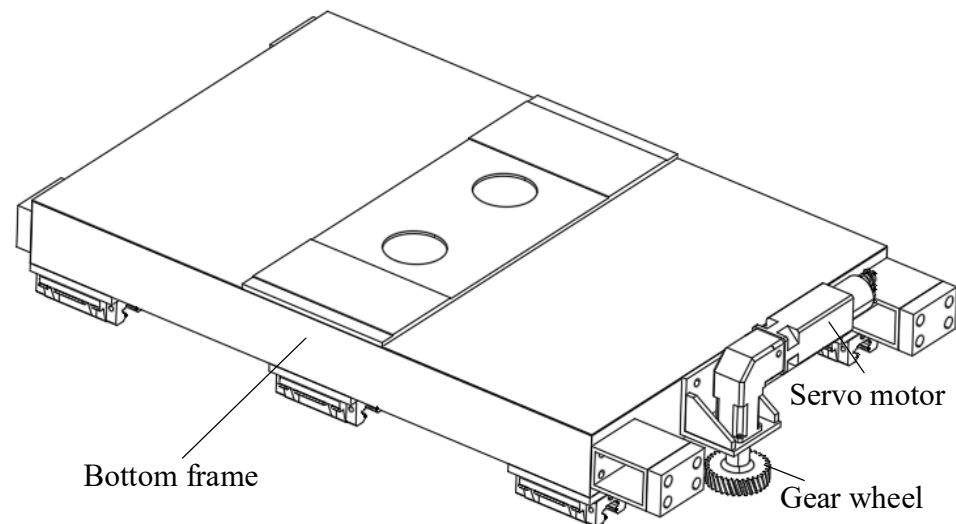


Figure 3. Structure diagram of the axial movement joint.

In Figure 3, the bottom of the axial movement joint is connected to the guide rail on the base by means of a slider. The bottom frame of the axial movement joint adopts a frame structure and Q345 steel plate welding molding. Four cushion pads are installed on the two ends of the structural frame to slow the impact of the collision between the mechanical arms. The structural mounting surface is used to directly mount the vertical lifting joint module. It is driven by an AC servo motor and equipped with a multi-turn absolute encoder and electromagnetic brake. The precision planetary reducer is selected as the reducer, and hard face gear can effectively improve the wear resistance and reliability of the reducer.

3.2.2. Vertical Lifting Joint

The vertical lifting joint drives two sets of spiral lifts through the servo motor and the reducer to realize the lifting action of the robot, including the servo motor, the reducer, the T-bevel gear steering box, the coupling, the spiral lift, the guiding mechanism, and other parts, as shown in Figure 4.

In Figure 4, the vertical lifting joint is driven by the structural form of a servo motor and a reducer driving two spiral elevators. The two ends of the spiral elevator are vertically installed on the top of the base structure module. The middle is connected through a T-shaped bevel gear steering box. The bottom of the vertical lifting joint is directly installed on the axial moving joint module through bolts. The spiral elevator achieve lifting through the servo motor drive reducer and coupling. The guide mechanism adopts the shaft sleeve structure, which is mainly composed of the guide seat, the guide shaft, the end cover, etc., which is used to provide reliable guidance for the screw lift in the lifting action and ensure the linearity and stability of the lifting action. The flange mounting surface and the end cover of the guide mechanism are directly connected with the vertical moving joint, which drives the radial moving joint and the circular rolling joint to lift simultaneously when the lift is lifted.

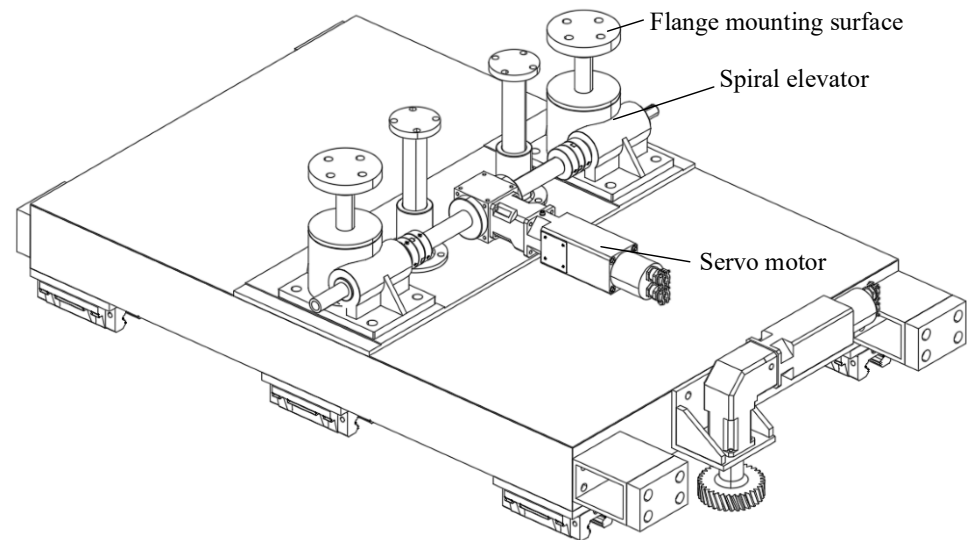


Figure 4. Structure diagram of the vertical lifting joint.

3.2.3. Radial Movement Joint

The radial movement joint drives the ball screw through the servo motor and the reducer to realize the radial movement function of the robot, including the servo motor, the reducer, the coupling, the ball screw, the connecting base, the top guide rail, the housing bracket, and other parts of the top view, as shown in Figure 5.

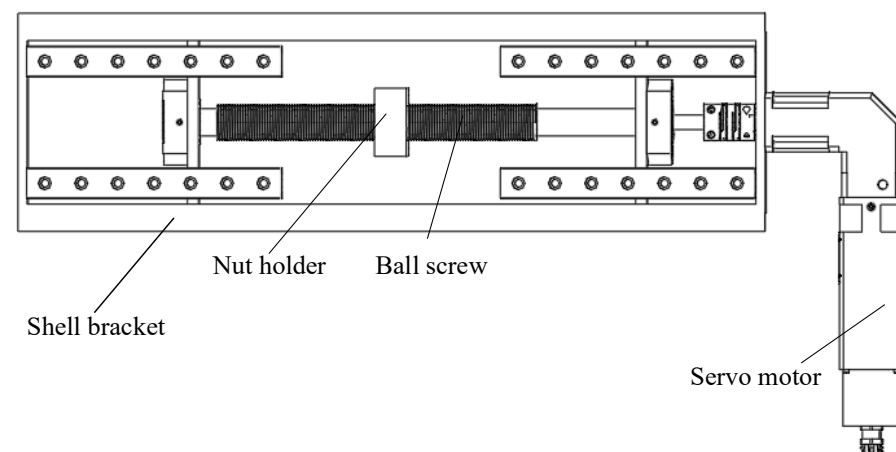


Figure 5. Top view of the radial prismatic joint structure.

In Figure 5, a lead screw is installed inside the shell bracket and a guide rail is installed on both sides of the top. The radial movement joint is connected to the bottom slider of the circular rolling joint through the top guide rail, and the middle is directly mechanically connected to the circular rolling joint through the nut holder. The servo motor drives the reducer to rotate, and the ball screw is driven by coupling. When the servo motor drives the ball screw to rotate, the circular rolling joint moves radially with the ball screw.

3.2.4. Circular Rolling Joint

The circular rolling joint realizes the circular rotation of the curved rolling body by driving the turbo worm mechanism and rack and pinion mechanism through the servo motor and the reducer, which mainly includes the servo motor and the reducer, turbo worm mechanism, curved rack, rolling bearing, curved rolling body, anti-static rubber, and rotation bracket, etc. The three-dimensional model of the circular rolling joint is shown in Figure 6.

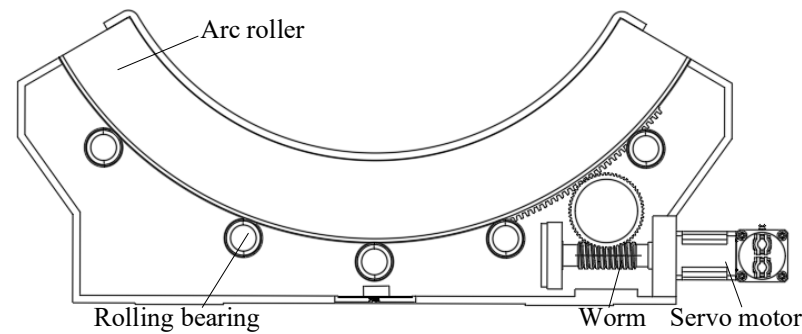


Figure 6. Frontal view of circular rolling joint.

In Figure 6, the arc roller is arranged on the top of the roll bracket as an arc structure matching the shape of the cabin workpiece, and the arc rack is arranged on the bottom side of the arc roller. The top circle diameter of the rack is larger than the top circle diameter of the turbine, and the rack engages with the turbine. When the servo motor and the reducer drive the worm gear to rotate, the rack action of the arc roller is driven by the gear of the turbine, and the circular rotation of the arc roller is realized. The rolling bearing is distributed in the inner cavity of the rolling bracket in an arc shape and rolls in contact with both sides of the bottom of the curved rolling body. The top of the arc roller is installed with curved anti-static material, which is in direct contact with the cabin workpiece.

3.3. Strength Analysis of Key Components

Strength analysis and strength checks of key components are indispensable links in the design of mechanical systems, aiming to theoretically ensure the stiffness and mechanical reliability of the overall mechanism. Strength analysis is required in the process of robot research and development and design [11–13]. Since the robot is self-heavy and the workpiece size and weight of the robot are large, it is necessary to analyze the strength of the main load-bearing components of the robot. The main load-bearing parts of the cabin docking robot include the base of the axial moving joint, the spiral elevator of the vertical lifting joint, the external shell of the radial moving joint, and the rolling bearing of the circular rolling joint.

The Simcenter Nastran 8031 software module of NX 2023 software is used to analyze the static stress of the main load-bearing components, assuming that the weight of the cabin workpiece is set to 1000 kg, and the weight of the actual key components is added as the working load. At the same time, the material of each key component is Q345 steel or 45 steel.

3.3.1. Strength Analysis of the Bottom Frame

The bottom frame of the axial moving joint is the load-bearing part of the whole robot, which is used to support the vertical lifting joint, the radial moving joint, the circular rolling joint, and the load workpiece. In order to simulate the stress of the axial moving joint frame, the force grid and nodes are divided, and the two mounting seats are set as the stress points, which is consistent with the actual situation. Six slider mounting positions are added at the bottom as fixed constraints, as shown in Figure 7. The bottom frame is 1200 mm long, 150 mm high, and 820 mm wide.

Taking the total gravity of 13 kN as the working load, the static stress analysis is carried out. The equivalent stress, elastic deformation, and total strain results of the bottom frame are shown in Figure 8.

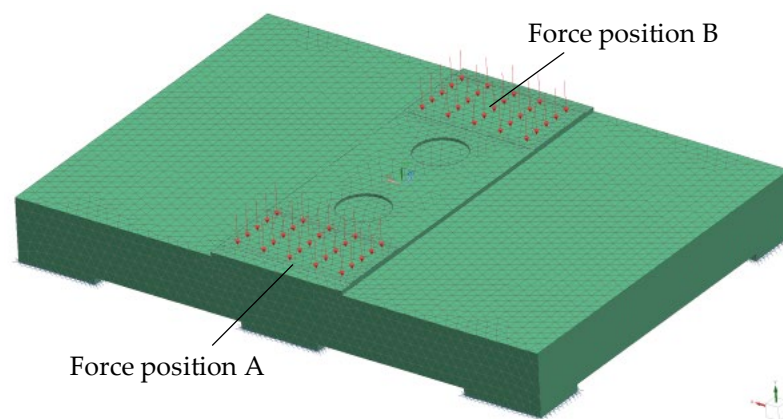
As can be seen in Figure 8, the maximum equivalent stress on the bottom frame is 31.81 MPa, and the maximum total deformation is 0.125 mm. Because the bottom frame is made of Q345 steel, the yield limit is 345 MPa, and the safety factor of anti-instability is 5. The allowable stress of the bottom frame is much greater than its maximum equivalent stress, and the design is reasonable.

3.3.2. Strength Analysis of the Spiral Elevator

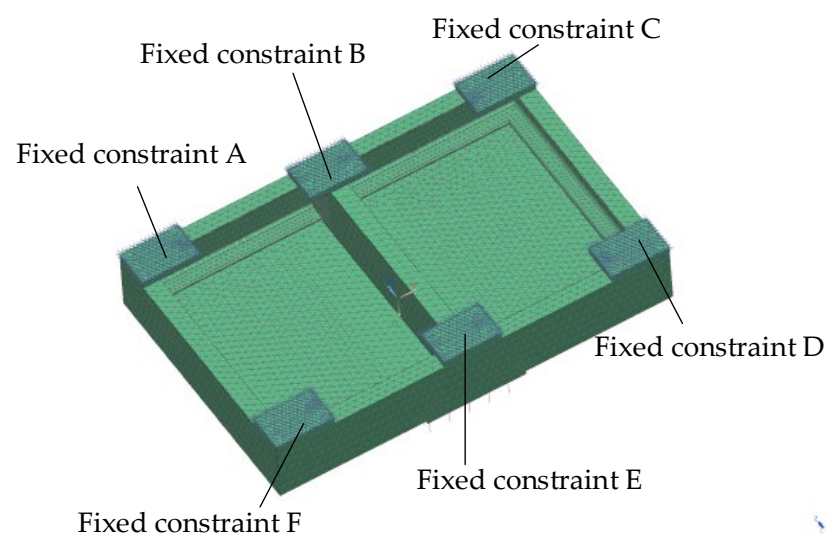
The spiral elevator of the vertical lifting joint supports the radial movement joint, the circular rolling joint, and the load weight through the mounting surface at the top, which is the main bearing part of the vertical lifting joint. In order to simulate the stress situation of the spiral elevator, the stress grid and nodes are divided, and the installation surface of the end flange of the trapezoid lead screw inside the elevator is taken as the stress point, which is consistent with the actual situation. Add the bottom of the lead screw as a fixed constraint, as shown in Figure 9. The stroke of the trapezoidal lead screw is 150 mm, and the diameter of the lead screw is 30 mm.

Taking the total gravity of 11 kN as the working load, the static stress analysis is carried out. The results of the effect force, elastic deformation, and total strain of the trapezoid lead screw inside the spiral elevator are shown in Figure 10.

As can be seen in Figure 10, the maximum equivalent stress of the trapezoidal screw inside the spiral lift is 28.86 MPa, and the maximum total deformation is 0.0177 mm. The trapezoidal screw is made of 45 steel, the yield limit is 355 MPa, and the safety factor of anti-instability is selected to be 5. The allowable stress of the spiral lift is much greater than its maximum equivalent stress, and the design is reasonable.

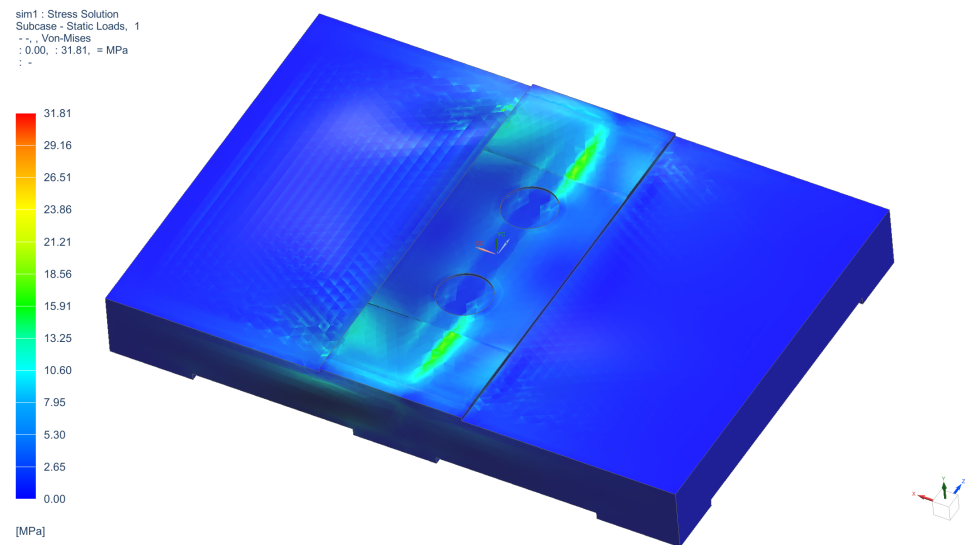


(a) Setting of force points on the bottom frame

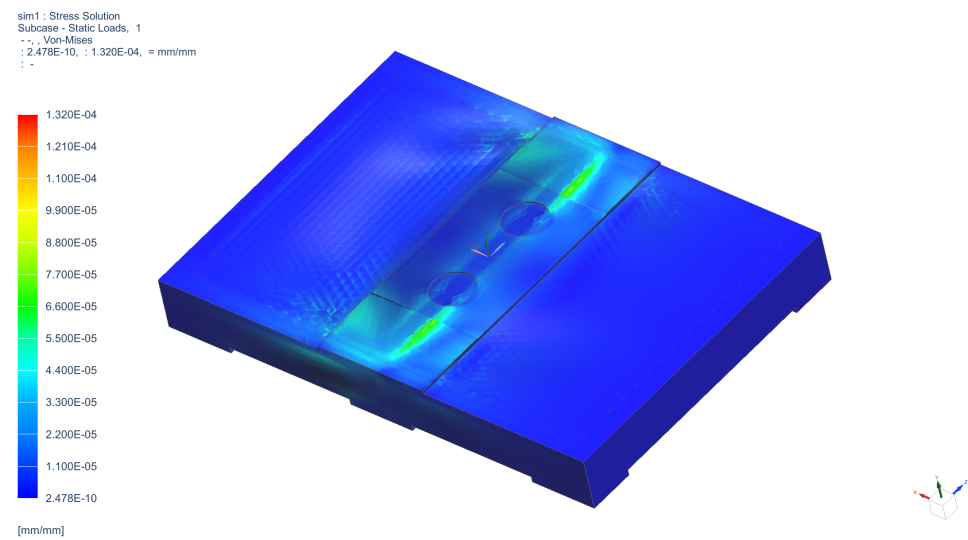


(b) Setting of fixed constraints on the bottom frame

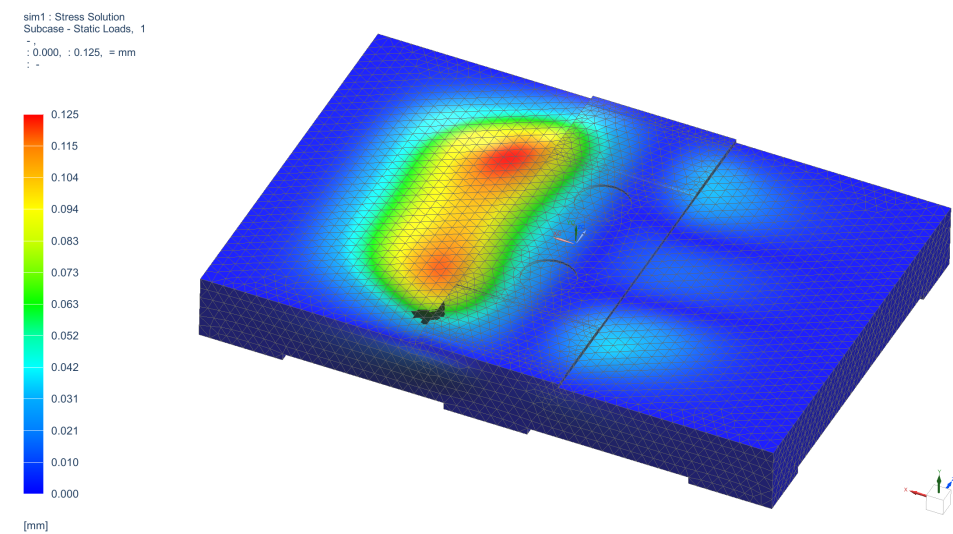
Figure 7. Simulation setting of the bottom frame of the axial moving joint.



(a) Equal effect diagram of the bottom frame



(b) Elastic deformation diagram of the bottom frame



(c) Total strain diagram of the bottom frame

Figure 8. Static stress analysis results of the bottom frame.

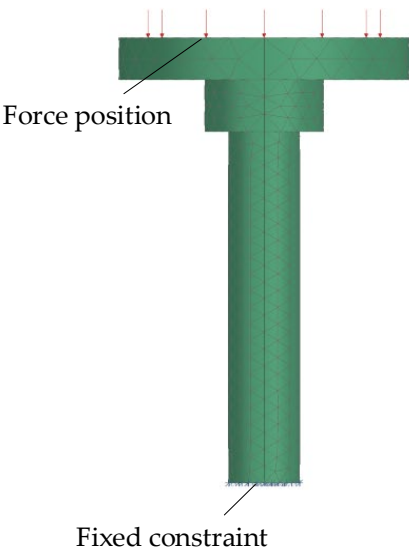
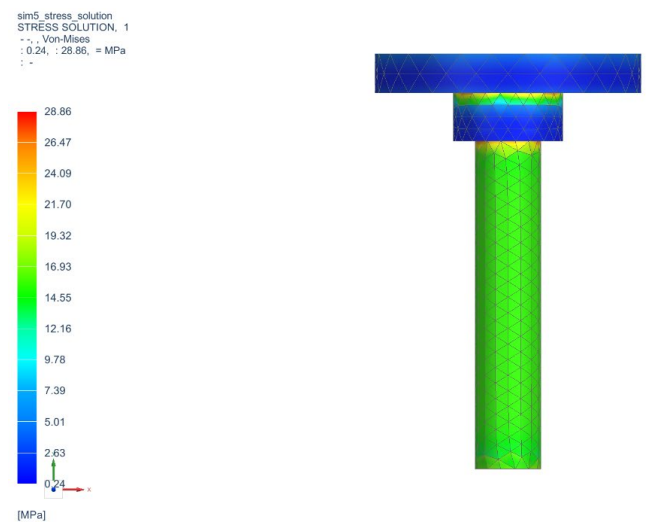
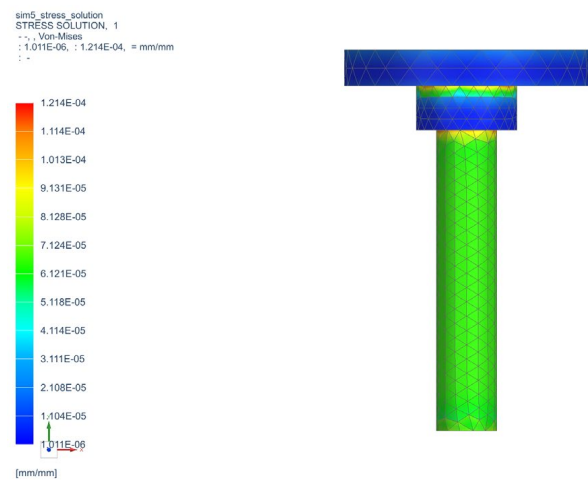


Figure 9. Setting of the force point and fixed constraint of the trapezoidal lead screw.

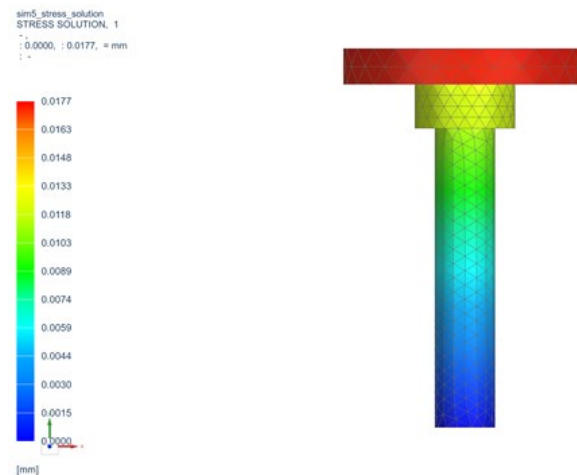


(a) Equal effect diagram of the trapezoidal lead screw in the spiral elevator



(b) Elastic deformation diagram of the trapezoid lead screw in the spiral elevator

Figure 10. Cont.



(c) Total strain diagram of the trapezoidal screw inside the spiral elevator

Figure 10. Static stress simulation results of the trapezoidal lead screw.

3.3.3. Strength Analysis of the Shell Bracket

The upper part of the shell bracket of the radial mobile joint is installed with a top guide rail, which is used to support the upper mounting mechanism and load, and is an important load-bearing part of the whole robot. In order to simulate the stress of the radial moving joint, the force grid and nodes are divided, and the installation positions of the four top guide rails are taken as the stress points, which are consistent with the actual situation. The top mounting position of the bottom two spiral lifts are added as a fixed constraint, as shown in Figure 11. The length of the shell bracket is 820 mm, the width is 240 mm, and the height is 115 mm.

Taking the total gravity of 10.2 kN as the working load, the static stress analysis is carried out. The equivalent stress, elastic deformation, and total strain results of the radial movement joint shell bracket are shown in Figure 12.

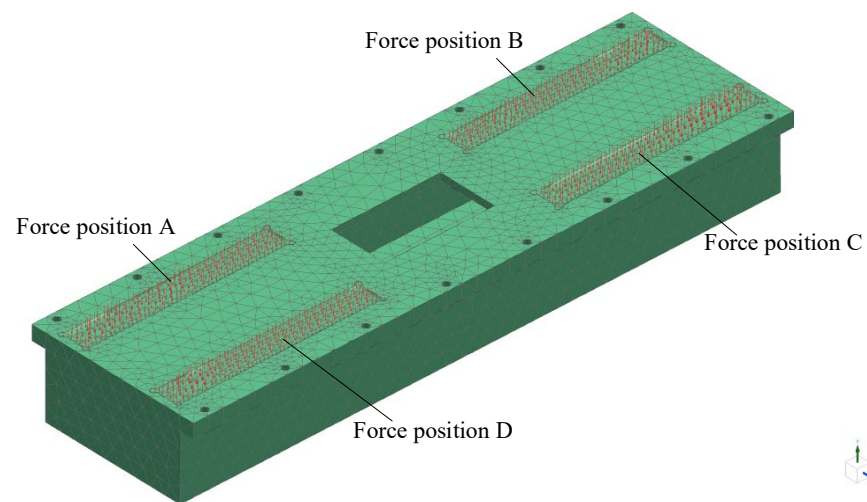
As can be seen in Figure 12, the maximum equivalent stress on the shell bracket is 23.13 MPa, and the maximum total deformation is 0.0182 mm. Because the shell bracket is made of Q345 steel, the yield limit is 345 MPa, and the safety factor of anti-instability is 5. The allowable stress of the shell bracket is much greater than its maximum equivalent stress, and the design is reasonable.

3.3.4. Strength Analysis of the Rolling Bearing

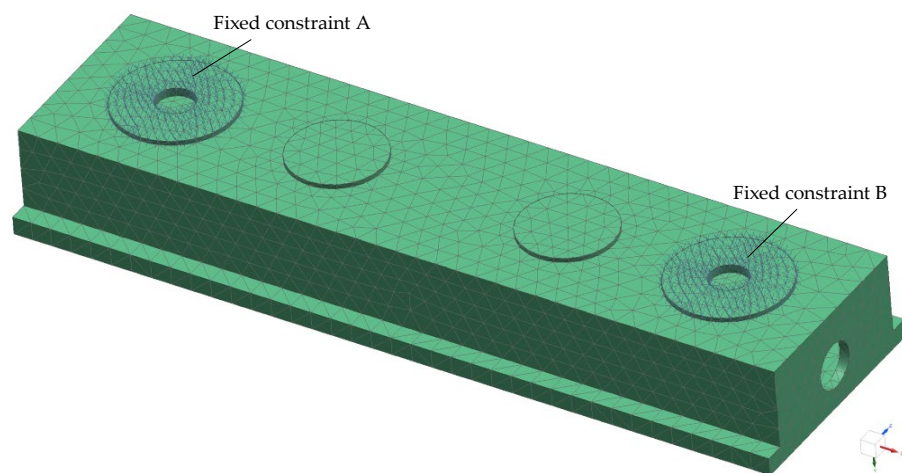
The rolling bearing of the circular rolling joint is connected to the curved rolling body to support the load and is an important bearing part of the robot. In order to simulate the stress situation of the rolling bearing with circular rolling joints, the stress grid and nodes are divided, and the contact position between the middle of the rolling bearing and the curved rolling body is taken as the stress point, which is consistent with the actual situation. The limit positions at both ends are added as fixed constraints, as shown in Figure 13. The diameter of the rolling bearing is 25 mm, and the length is 165 mm.

Taking the total gravity of 10 kN as the working load, the static stress analysis is carried out. The equivalent stress, elastic deformation, and total strain results of the circular rolling joint rolling bearing are shown in Figure 14.

As can be seen in Figure 14, the maximum equivalent stress on the rolling bearing is 9.153 MPa, and the maximum total deformation is 0.001195 mm. Because the rolling bearing is made of 45 steel, the yield limit is 355 MPa, and the anti-instability safety factor is 5. The allowable stress of the rolling bearing is much greater than its maximum equivalent stress, and the design is reasonable.

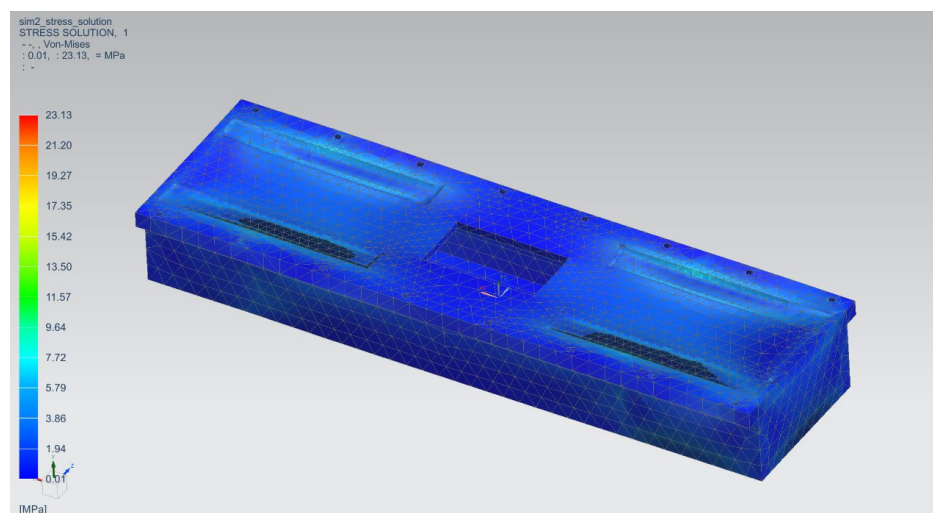


(a) Setting of the force points of the shell bracket



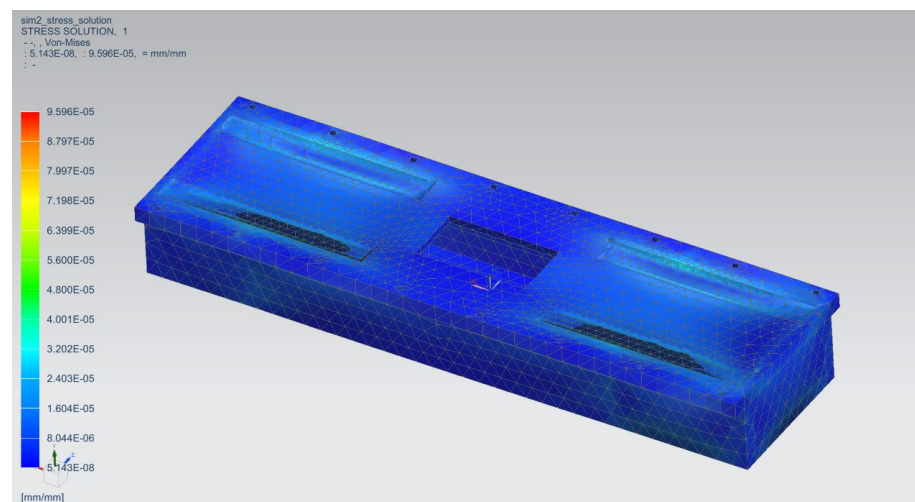
(b) Fixed constraint setting of the shell bracket

Figure 11. Loading point and fixed constraint setting of the shell bracket.

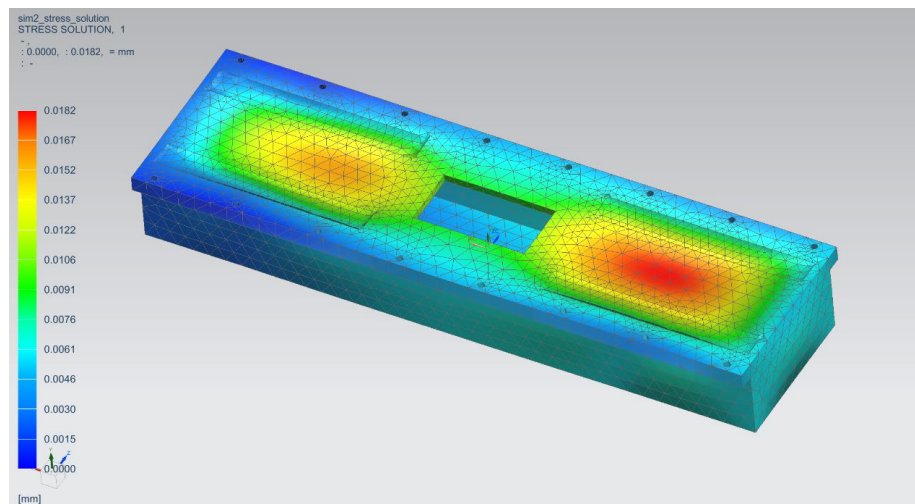


(a) Equal effect diagram of the shell bracket

Figure 12. Cont.



(b) Elastic deformation diagram of the shell bracket



(c) Total strain diagram of the shell bracket

Figure 12. Static stress simulation of the shell bracket.

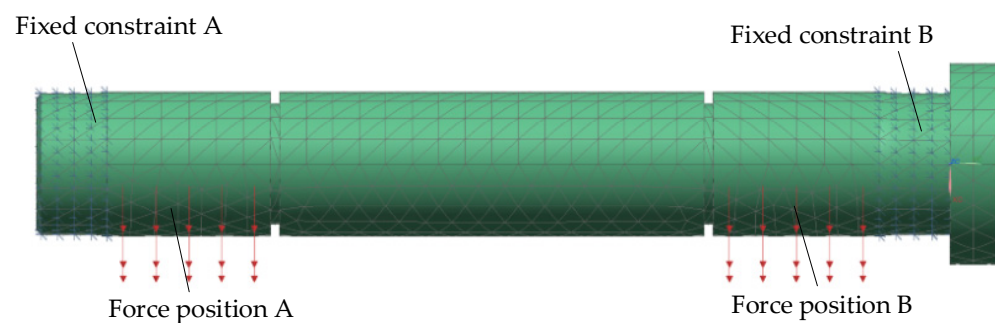
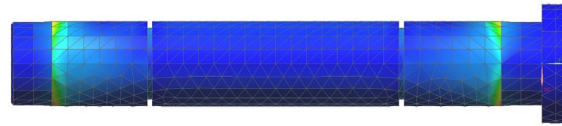


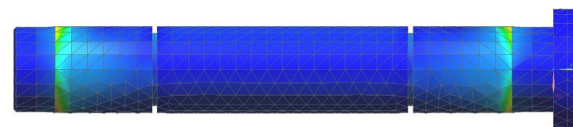
Figure 13. Setting of the force point and fixed constraint of the rolling bearing.

sim3 : Stress Solution
Subcase - Static Loads, 1
:-, : Von-Mises
: 0.001, : 9.153, = MPa
:-



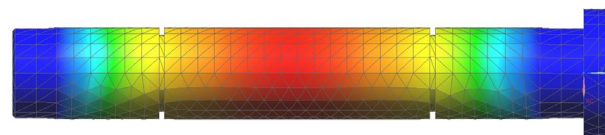
(a) Equal effect diagram of the rolling bearing

sim3 : Stress Solution
Subcase - Static Loads, 1
:-, : Von-Mises
: 5.845E-09, : 6.044E-05, = mm/mm
:-



(b) Elastic deformation diagram of the rolling bearing

sim3 : Stress Solution
Subcase - Static Loads, 1
:-, : 0.000E+00, : 1.195E-03, = mm
:-



(c) Total strain diagram of the rolling bearing

Figure 14. Static stress simulation results of the rolling bearing.

4. Kinematics Modeling and Simulation Verification

4.1. Kinematics Modeling

4.1.1. Kinematics Modeling of the Cabin Docking Robot System

Kinematics analysis is the basis of robot design. In order to facilitate the kinematics analysis of the robot, a schematic diagram of the docking robot mechanism in the cabin is shown in Figure 15.

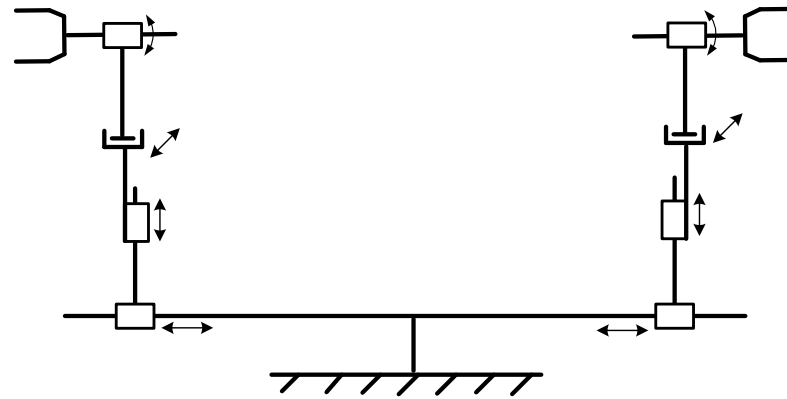


Figure 15. Schematic diagram of the docking robot mechanism in the cabin segment.

In Figure 15, the robot system is composed of left and right robotic arms, each of which is composed of four degrees of freedom, and from bottom to top are axial moving joints, vertical lifting joints, radial moving joints, and circular rolling joints. Two robotic arms are composed to coordinate the space attitude adjustment of the cabin workpiece.

The D-H (Denavit–Hartenberg) model [14,15] uses four parameters (rod length, zero position, bias, and torsion angle) to characterize the spatial coordinate positioning of a single joint, which is widely used in robot calibration, robot control, and trajectory planning [16–20]. According to the D-H modeling method, the joint coordinate system of the module docking robot is established, as shown in Figure 16.

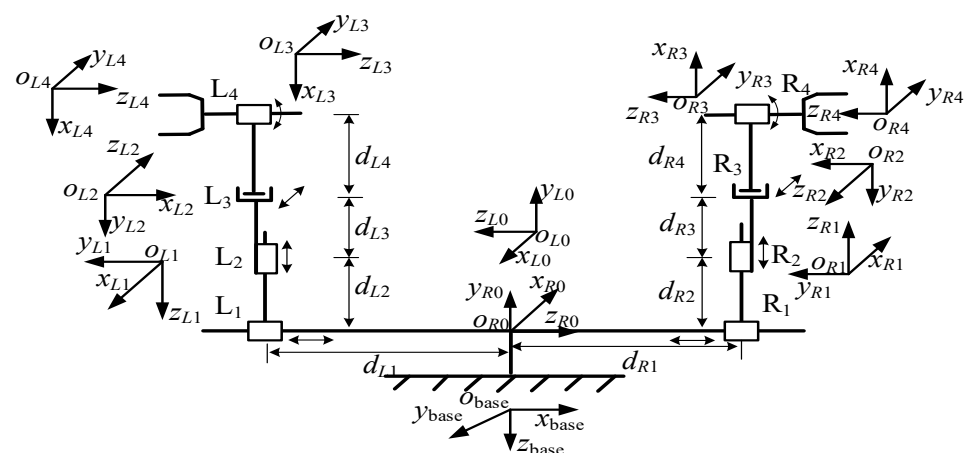


Figure 16. Schematic diagram of connecting rod coordinate system of the docking robot.

The base coordinate system is represented by $O_{base}(x_{base}, y_{base}, z_{base})$, and the coordinate system of the left robot arm $O_{L0}(x_{L0}, y_{L0}, z_{L0})$ and the coordinate system of the right robot arm $O_{R0}(x_{R0}, y_{R0}, z_{R0})$ are established in the middle position of the two robot arms on the base guide rail. Coordinate system $O_{L1}(x_{L1}, y_{L1}, z_{L1})$, coordinate system $O_{L2}(x_{L2}, y_{L2}, z_{L2})$, coordinate system $O_{L3}(x_{L3}, y_{L3}, z_{L3})$, and coordinate system $O_{L4}(x_{L4}, y_{L4}, z_{L4})$ are respectively established for the axial moving joint, vertical lifting joint, left and right moving joint, and circular rolling joint of the left mechanical arm.

Coordinate system $O_{R1}(x_{R1}, y_{R1}, z_{R1})$, coordinate system $O_{R2}(x_{R2}, y_{R2}, z_{R2})$, coordinate system $O_{R3}(x_{R3}, y_{R3}, z_{R3})$ and coordinate system $O_{R4}(x_{R4}, y_{R4}, z_{R4})$ are respectively established for the axial moving joint, vertical lifting joint, left and right moving joint and circular rolling joint of the left mechanical arm.

In Figure 16, each joint is described by the joint angle, connecting rod offset, connecting rod length, and connecting rod angle. The D-H parameters of the cabin docking robot are obtained, as shown in Table 2.

Table 2. D-H parameters of the docking robot.

Link	Joint Angle θ_i	Link Offset d_i	Link Length a_i	Link Angle α_i
Base-L ₀	$\pi/2$	0	0	$-\pi/2$
L ₁	0	$d_{L1} + 625$	0	$\pi/2$
L ₂	$-\pi/2$	$d_{L2} + 140$	0	$\pi/2$
L ₃	$\pi/2$	d_{L3}	600	$\pi/2$
L ₄	θ_L	-470	0	0
Base-R ₀	$\pi/2$	0	0	$\pi/2$
R ₁	0	$d_{R1} + 625$	0	$-\pi/2$
R ₂	$\pi/2$	$d_{R2} + 140$	0	$-\pi/2$
R ₃	$-\pi/2$	d_{R3}	600	$-\pi/2$
R ₄	θ_R	-470	0	0

The forward kinematics equations of the right robotic arm of the cabin docking robot are obtained according to the spatial pose matrix calculation, as shown in Equation (1). The forward kinematics equations of the left robotic arm of the cabin docking are shown in Equation (2).

$$\begin{aligned}
 p_{Rx} &= d_{R1} + 1095 \\
 p_{Ry} &= -d_{R3} \\
 p_{Rz} &= d_{R2} + 740 \\
 y_R &= -\theta_R
 \end{aligned} \tag{1}$$

where p_{Rx} , p_{Ry} , p_{Rz} , and y_R represent the coordinate variables of the X-axis direction, Y-axis direction, Z-axis direction, and circumferential direction of the operating space of the right robotic arm, respectively.

$$\begin{aligned}
 p_{Lx} &= -d_{L1} - 1095 \\
 p_{Ly} &= -d_{L3} \\
 p_{Lz} &= d_{L2} + 740 \\
 y_L &= 180 + \theta_L
 \end{aligned} \tag{2}$$

where p_{Lx} , p_{Ly} , p_{Lz} , and y_L represent the coordinate variables of the X-axis direction, Y-axis direction, Z-axis direction, and circumferential direction of the operating space of the left robotic arm, respectively.

According to the mapping relationship of Equations (1) and (2), the inverse kinematics transformation equations of the right robotic arm and the left robotic arm of the cabin docking can be established, respectively, as shown in Equations (3) and (4).

$$\begin{aligned}
 d_{R1} &= p_{Rx} - 1095 \\
 d_{R3} &= -p_{Ry} \\
 d_{R2} &= p_{Rz} - 740 \\
 \theta_R &= -y_R
 \end{aligned} \tag{3}$$

$$\begin{aligned}
 d_{L1} &= -p_{Lx} - 1095 \\
 d_{L3} &= -p_{Ly} \\
 d_{L2} &= p_{Lz} - 740 \\
 \theta_L &= y_L - 180
 \end{aligned} \tag{4}$$

4.1.2. Joint Kinematics Modeling of the Cabin Docking Robot and Cabin Workpiece

In order to analyze the attitude adjustment process of the cabin workpiece carried out by the cabin docking robot, the end coordinate system $O_L(x_L, y_L, z_L)$ of the left robotic arm for cabin docking, the end coordinate system $O_R(x_R, y_R, z_R)$ of the right robotic arm for cabin docking, the base coordinate system $O_{base}(x_{base}, y_{base}, z_{base})$, the center coordinate system $O_1(x_1, y_1, z_1)$ of the left end face of the cabin workpiece, and the center coordinate system $O_2(x_2, y_2, z_2)$ of the right end face of the cabin workpiece are established.

Suppose that the distance between coordinate system $O_1(x_1, y_1, z_1)$ and the origin of coordinate system $O_L(x_L, y_L, z_L)$ is D_1 , the distance between coordinate system $O_L(x_L, y_L, z_L)$ and the origin of coordinate system $O_R(x_R, y_R, z_R)$ is D_2 , and the distance between coordinate system $O_R(x_R, y_R, z_R)$ and the origin of coordinate system $O_2(x_2, y_2, z_2)$ is D_3 , as shown in Figure 17.

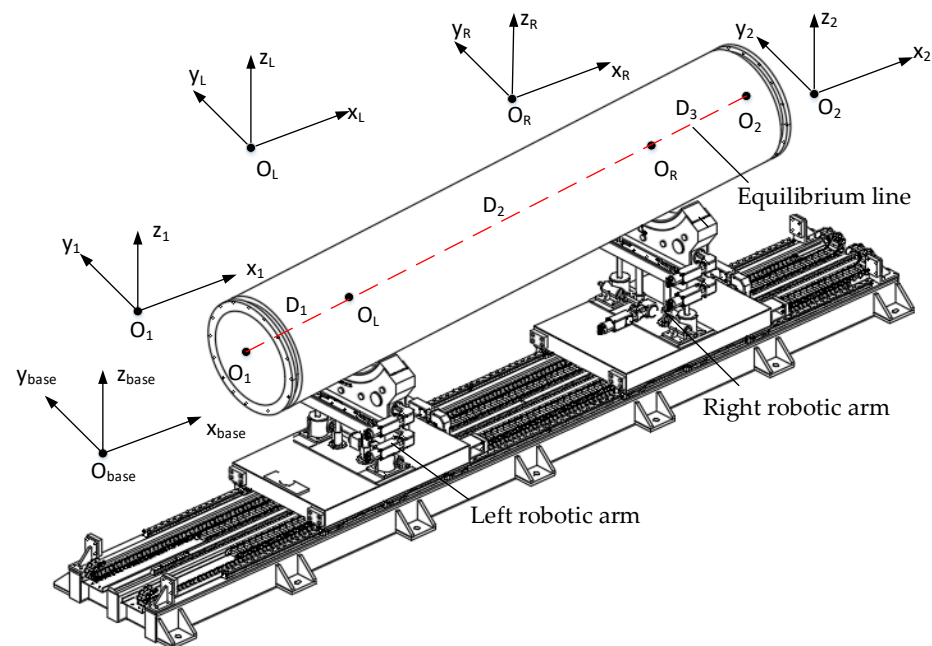


Figure 17. Distribution of each coordinate system of the docking two-arm robot in the cabin segment.

In Figure 17, the movement direction of the axial moving joints of the cabin docking robot is defined as the X-axis direction of the coordinate system, the movement direction of the left and right moving joints of the cabin docking robot is defined as the Y-axis direction of the coordinate system, and the movement direction of the vertical lifting joints of the cabin docking robot is defined as the Z-axis direction of the coordinate system. According to the coordinate system established in Figure 17, the definition of pitch angle, yaw angle, and rolling angle of the cabin workpiece is shown in Figure 18.

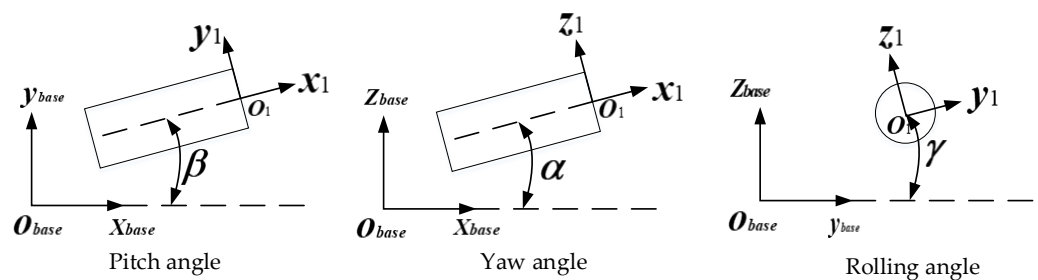


Figure 18. Definition of the attitude parameters of the cabin workpiece.

The relationship between the pose of the cabin workpiece and the coordinate system of the cabin docking robot can be analyzed in four situations as follows: the initial equilibrium

position, the pitch angle is not at 0° , the yaw angle is not at 0° , and the roll angle is not at 0° . The detailed description is as follows:

(1) Initial equilibrium position

In the actual production process, it is generally required that the cabin docking robot is in a balanced spatial posture. The end coordinate system $O_L(x_L, y_L, z_L)$ of the left robotic arm for cabin docking, the end coordinate system $O_R(x_R, y_R, z_R)$ of the right robotic arm for cabin docking, the base coordinate system $O_{base}(x_{base}, y_{base}, z_{base})$, the center coordinate system $O_1(x_1, y_1, z_1)$ of the left end face of the cabin workpiece, and the center coordinate system $O_2(x_2, y_2, z_2)$ of the right end face of the cabin workpiece are established.

Their origin is in a straight line, and the pitch angle, yaw angle, and rolling angle of the cabin workpiece are 0° , as shown in Figure 19.

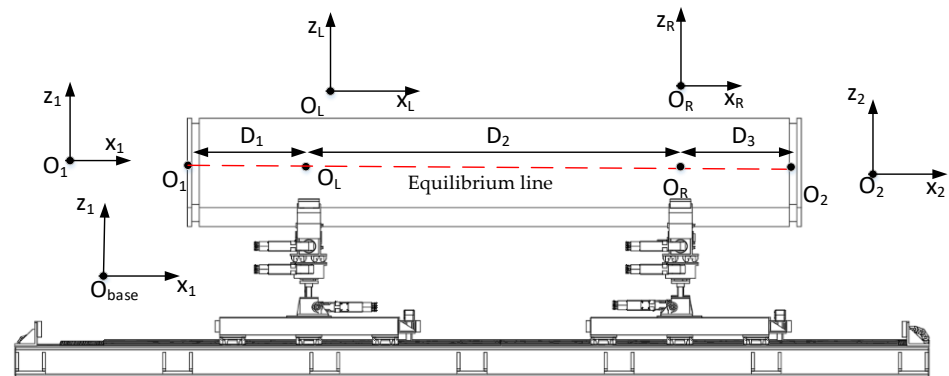


Figure 19. Coordinate system of the docking robot during the initial equilibrium position.

In Figure 19, when the cabin docking two-arm robot is in the initial equilibrium position, the values of coordinate systems $O_1(x_1, y_1, z_1)$, $O_L(x_L, y_L, z_L)$, $O_R(x_R, y_R, z_R)$, and $O_2(x_2, y_2, z_2)$ are equal in the X-direction and Y-direction. The position relationship of the coordinate system in the Z-direction is shown in Equation (5).

$$\begin{cases} (z_1 - z_L)^2 = D_1^2 \\ (z_L - z_R)^2 = D_2^2 \\ (z_R - z_2)^2 = D_3^2 \end{cases} \quad (5)$$

(2) The pitch angle of the cabin workpiece is not 0°

Because of the influence of friction between the docking robot and the cabin workpiece, and the limited stroke of the vertical lifting joint of the docking robot (± 50 mm), when the pitch angle α changes, the docking robot still makes contact with the cabin workpiece. Therefore, the origin of the coordinate system O_L at the end of the left robotic arm of the cabin docking, the coordinate system O_R at the end of the right robotic arm of the cabin docking, the center coordinate system O_1 at the left end face of the cabin workpiece, and the center coordinate system O_2 at the right end face of the cabin workpiece are approximately in a straight line, as shown in Figure 20.

In Figure 20, when the pitch angle α is not 0, the values of coordinate systems $O_1(x_1, y_1, z_1)$, $O_L(x_L, y_L, z_L)$, $O_R(x_R, y_R, z_R)$ and $O_2(x_2, y_2, z_2)$ in the Y-direction are equal, and the position relationship of each coordinate system is shown in Equation (6).

$$\begin{cases} (x_1 - x_L)^2 + (z_1 - z_L)^2 = D_1^2 \\ (x_1 - x_R)^2 + (z_L - z_R)^2 = D_2^2 \\ (x_R - x_2)^2 + (z_R - z_2)^2 = D_3^2 \end{cases} \quad (6)$$

The relationship between the pitch angle α and the coordinate system parameters is shown in Equation (7).

$$\sin(\alpha) = \frac{z_R - z_L}{D_2} \quad (7)$$

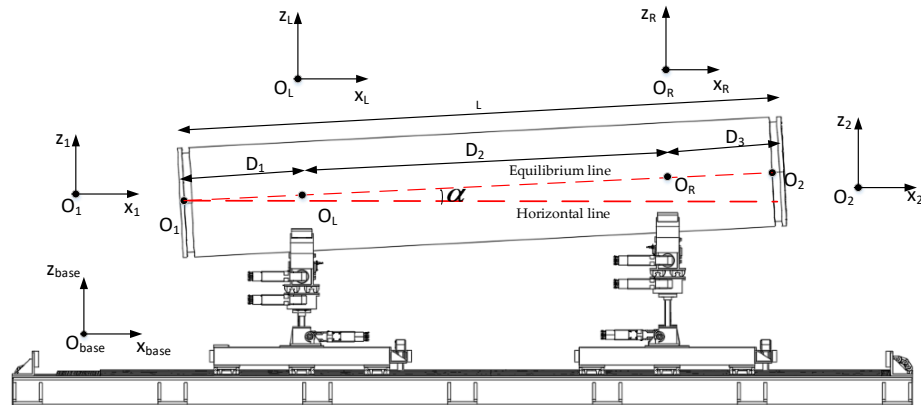


Figure 20. Case of the coordinate system when the pitch angle is not 0° .

(3) The yaw angle of the cabin workpiece is not 0°

Because of the influence of friction between the docking robot and the cabin workpiece, and the limited stroke of the radial movement joint of the docking robot (± 50 mm), when the pitch angle α changes, the docking robot still makes contact with the cabin workpiece. Therefore, the origin of the coordinate system O_L at the end of the left robotic arm of the cabin docking, the coordinate system O_R at the end of the right robotic arm of the cabin docking, the center coordinate system O_1 at the left end face of the cabin workpiece, and the center coordinate system O_2 at the right end face of the cabin workpiece are approximately in a straight line, as shown in Figure 21.

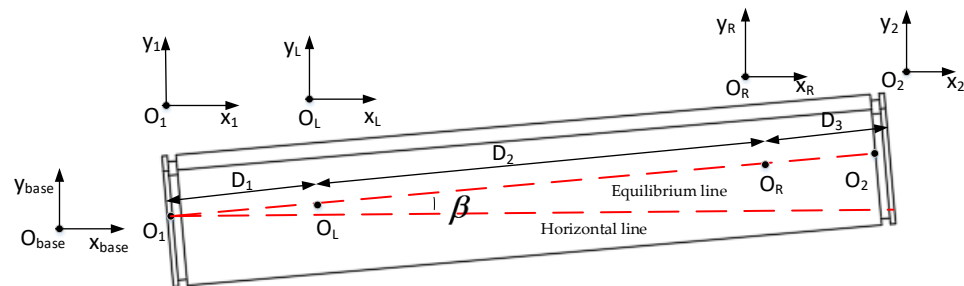


Figure 21. Case of the coordinate system when the yaw angle is not 0° .

In Figure 21, when the yaw angle β is not 0, the values of coordinate systems $O_1(x_1, y_1, z_1)$, $O_L(x_L, y_L, z_L)$, $O_R(x_R, y_R, z_R)$, and $O_2(x_2, y_2, z_2)$ in the Z-direction are equal, and the position relationship of each coordinate system is shown in Equation (8).

$$\begin{cases} (x_1 - x_L)^2 + (y_1 - y_L)^2 = D_1^2 \\ (x_1 - x_R)^2 + (y_L - y_R)^2 = D_2^2 \\ (x_R - x_2)^2 + (y_R - y_2)^2 = D_3^2 \end{cases} \quad (8)$$

The relationship between the yaw angle and the coordinate system parameters is shown in Equation (9).

$$\sin(\beta) = \frac{y_R - y_L}{D_2} \quad (9)$$

- (4) The rolling angle of the cabin workpiece γ is not 0°

Because the workpiece of the cabin belongs to rigid body, the position relation of each coordinate system is not affected when the rolling angle changes. Therefore, the origin of the coordinate system O_L at the end of the left robotic arm of the cabin docking, the coordinate system O_R at the end of the right robotic arm of the cabin docking, the center coordinate system O_1 at the left end face of the cabin workpiece, and the center coordinate system O_2 at the right end face of the cabin workpiece are approximately in a straight line, as shown in Figure 22.

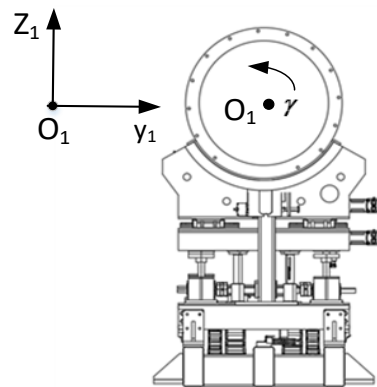


Figure 22. Case of the coordinate system when the rolling angle is not 0° .

In Figure 22, when the rolling angle γ of the cabin workpiece is not 0, the position relationship of each coordinate system is the same as the initial equilibrium position.

Therefore, according to the above analysis results, the following conclusions can be drawn:

- (1) When the attitude of the module changes, the relative distance between the origin of the coordinate system at the end of the left robotic arm of the module docking and the origin of the coordinate system at the end of the right robotic arm of the module docking remains unchanged.
- (2) When the cabin roll angle changes, the position adjustment of the cabin docking robot is not affected, but the attitude of the cabin itself is affected.

Assuming that the motion trajectory of the end of the left robotic arm is represented by $K_L(x_L(t), y_L(t), z_L(t))$, and the motion trajectory of the end of the right robotic arm is represented by $K_R(x_R(t), y_R(t), z_R(t))$, the first equation of the joint kinematics model is obtained:

$$(x_L(t) - x_R(t))^2 + (y_L(t) - y_R(t))^2 + (z_L(t) - z_R(t))^2 = D_2^2 \quad (10)$$

In Equation (10), the adjustment of the space position of the cabin is based on the movement trajectory $K_L(x_L(t), y_L(t), z_L(t))$ of the end of the left robotic arm of the cabin docking. The movement trajectory $K_R(x_R(t), y_R(t), z_R(t))$ of the end of the right robotic arm of the cabin docking follows the movement of the left robotic arm, and the relative distance from the movement trajectory of the end of the left robotic arm is guaranteed to remain unchanged.

In addition to participating in the adjustment of the space position, the right robotic arm of cabin docking is also adjusted for the attitude of the cabin. In this way, the movement trajectory $K_R(x_R(t), y_R(t), z_R(t))$ of the end of the right robotic arm of cabin docking can be divided into two parts, respectively assumed to be $K_R^1(x_R(t), y_R(t), z_R(t))$ and $K_R^2(x_R(t), y_R(t), z_R(t))$. The relationship is as follows:

$$K_R(x_R(t), y_R(t), z_R(t)) = K_R^1(x_R(t)^1, y_R(t)^1, z_R(t)^1) + K_R^2(x_R(t)^2, y_R(t)^2, z_R(t)^2) \quad (11)$$

In Equation (11), A is used to follow the action of the left robotic arm, and B reflects the attitude change in the cabin segment. The following equation exists:

$$\begin{cases} x_R(t)^2 = x_L(t) + D_2 \cos(\alpha(t)) \cos(\beta(t)) \\ y_R(t)^2 = y_L(t) + D_2 \cos(\alpha(t)) \sin(\beta(t)) \\ z_R(t)^2 = z_L(t) + D_2 \cos(\alpha(t)) \end{cases} \quad (12)$$

where $\alpha(t)$ and $\beta(t)$ represent the yaw angle trajectory and the pitch angle trajectory of the cabin workpiece, respectively, and the motion trajectory of the yaw angle and pitch angle is reflected in the motion trajectory $K_R^2(x_R(t), y_R(t), z_R(t))$.

The coordinates of the end coordinate system $O_L(x_L, y_L, z_L)$ of the left robot arm are related to the coordinates $O_1(x_1, y_1, z_1)$ of the center of the end circle of the cabin workpiece. The second equation of the joint kinematics can be obtained as follows:

$$\begin{cases} x_L(t) = x_1 + D_1 \cos(\alpha(t)) \cos(\beta(t)) \\ y_L(t) = y_1 + D_1 \cos(\alpha(t)) \sin(\beta(t)) \\ z_L(t) = z_1 + D_1 \sin(\alpha(t)) \end{cases} \quad (13)$$

where $\alpha(t)$ and $\beta(t)$ are the pitch angle and yaw angle trajectories of the moving module, respectively.

4.2. Workspace Analysis

During the movement of the robotic arm, its travel is limited. The working space represents the reachable position of the reference point in the end mechanism of the robotic arm, and its size represents the spatial field of the movement of the robotic arm, which is one of the important indicators of the robotic arm [21]. According to the design parameters of the module docking robot in Table 1, and through the forward kinematics Equations (1) and (2) of the left and right robotic arms, the feasible domain in the working space is obtained, as shown in Table 3.

Table 3. Workspace analysis of the docking robot.

Serial Number	Item	Value
1	Left arm X-axis stroke	−1695~−495 mm
2	Left arm Y-axis stroke	−50~50 mm
3	Left arm Z-axis stroke	690~790 mm
4	Left arm rolling angle range	170~190°
5	Right arm X-axis stroke	495~1695 mm
6	Right arm Y-axis stroke	−50~50 mm
7	Right arm Z-axis stroke	690~790 mm
8	Right arm rolling angle stroke	−10~10°

The Monte Carlo method, also known as statistical simulation test method, estimates and describes the unknown characteristic quantity by sampling random variables and then determines its distribution [22]. This method is widely used to solve robot workspaces [23–25].

After the strain sample data are obtained through calculation, the sample data distribution is processed, and then the sample data are randomly simulated by the Monte Carlo method. The Monte Carlo method consists of the following steps:

- (1) Construct a probability model. In this paper, the probability distribution of the equivalent strain of the independent variable follows the normal distribution model.
- (2) Obtain sub-samples by simulation. Random numbers are generated within the constraints of each joint in the workspace according to the normal distribution, and the position in the operation space is obtained through the coordinate transformation relationship.

In this paper, the Monte Carlo method is used to carry out relevant operations through MATLAB 2021 software, and the working space of the designed robot arm is obtained. The cloud image of the working space of the robot arm obtained by this method is shown in Figures 23 and 24.

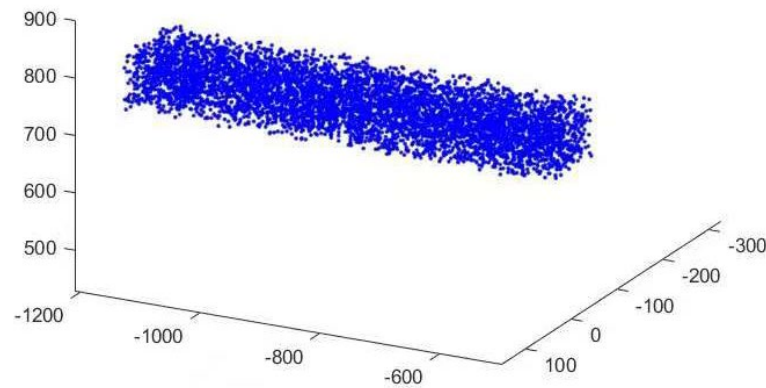


Figure 23. Working space cloud image of the left robotic arm.

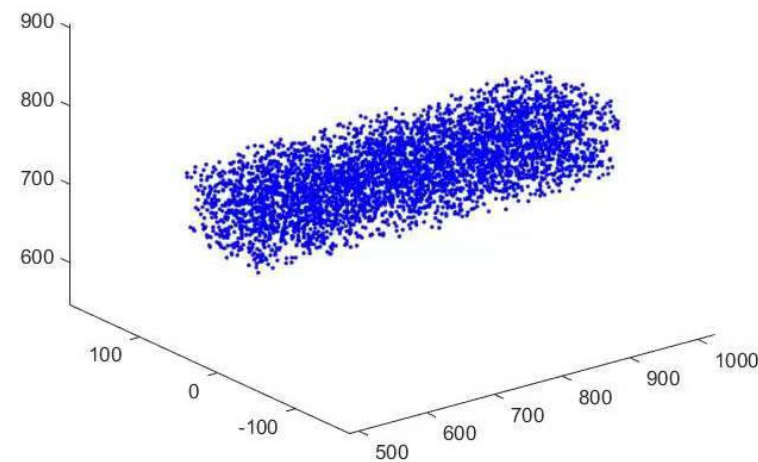


Figure 24. Working space cloud image of the right robotic arm.

4.3. Kinematics Simulation

4.3.1. Kinematics Simulation of Cabin Docking Robot System

Forward kinematics and inverse kinematics were verified by using Robotics Toolbox in MATLAB 2021 software.

(1) Establishment of simulation model

The Robotics Toolbox in MATLAB 2021 software was used to model the robot. The modeling process of the toolbox requires the D-H parameters of the robot as the basis, the LINK function and SerialLink function are used to realize the robot modeling, and the teach function is used to simulate and drive the robot to realize the visualization of the robot movement. The robot control panel is shown in Figure 25.

In Figure 25, the pose parameters (x, y, z, R, P, Y) of the corresponding end operating space of the robot arm can be changed by adjusting the joint space variables of the left robot arm or the joint space variables of the right robot arm. Meanwhile, the joint space variables of the robot arm are displayed graphically, as shown in Figure 26. The joint space variables q_2, q_3, q_4 , and q_5 of the left robotic arm correspond to d_{L1}, d_{L2}, d_{L3} , and θ_L , respectively, in Equation (6). The joint space variables q_2, q_3, q_4 , and q_5 of the right robotic arm correspond to d_{R1}, d_{R2}, d_{R3} , and θ_R and, respectively, in Equation (4).

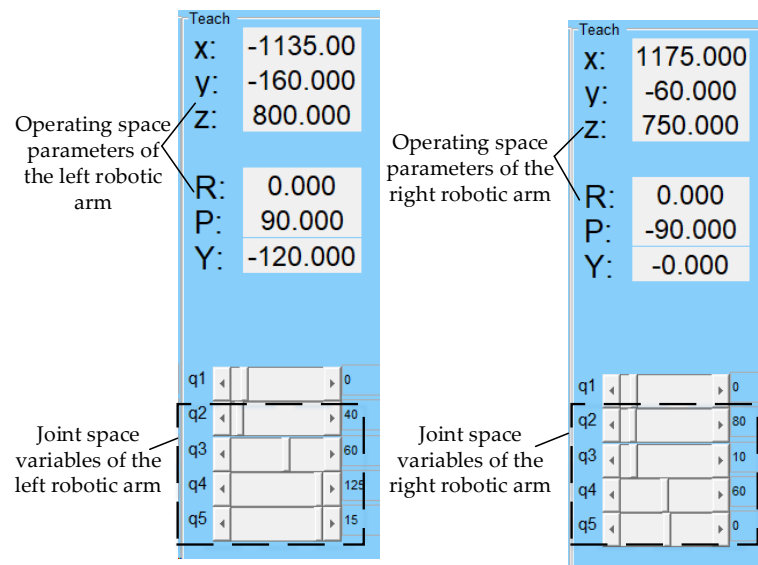


Figure 25. Control panel of the docking robot.

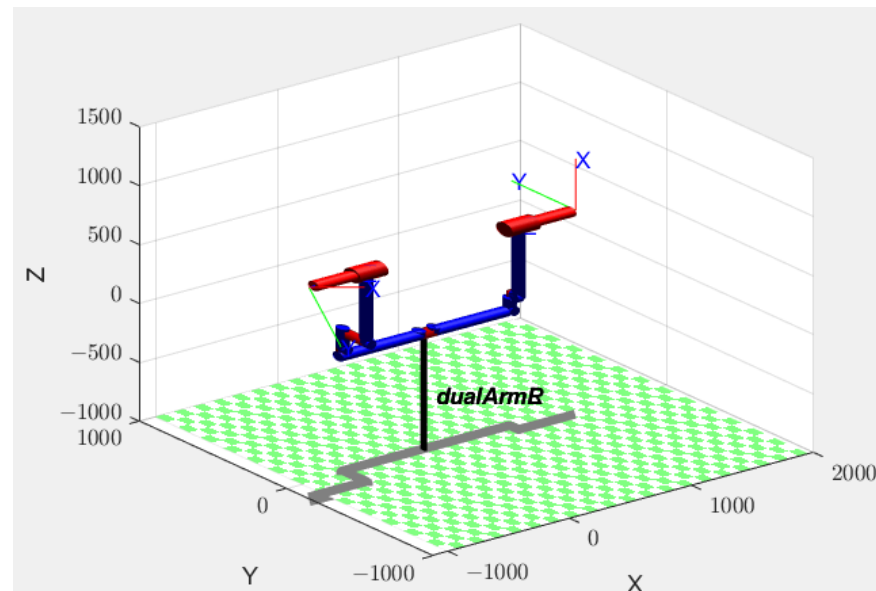


Figure 26. Three-dimensional space model of the docking robot.

(2) Kinematics simulation

Kinematics simulation process: First, the joint variables of the manipulator are given specific values, and the space pose parameters of the end of the manipulator are calculated by the forward kinematics Equations (4) and (6). Then, the spatial pose and pose parameters of the end of the robot arm are calculated through the inverse kinematics Equations (7) and (8) to obtain a new joint variable of the robot arm. The new joint variable is compared to the original joint variable to determine if they are equal. If the new joint variable is equal to the original, the forward and inverse kinematics modeling is proved correct; otherwise, it is proved incorrect, as shown in Figure 27.

According to the simulation ideas in Figure 27, the simulation process is as follows:

- (1) The joint variable $(d_{L1}, d_{L2}, d_{L3}, \theta_L)$ of the left robotic arm is $(40, 60, 30, -130)$, and the joint variable $(d_{R1}, d_{R2}, d_{R3}, \theta_R)$ of the right robotic arm is $(80, 20, 10, 30)$;
- (2) Through forward kinematics calculation, the end space pose (x_L, y_L, z_L, R, P, Y) of the left robotic arm is $(-1135, -30, 800, 0, 90, 50)$, and the end space pose (x_R, y_R, z_R, R, P, Y) of the right robotic arm is $(1175, -10, 760, 0, -90, -30)$;

- (3) The space pose of the end of the robot arm is brought into the inverse kinematics equation, and the calculated joint space variable $(d_{L1}, d_{L2}, d_{L3}, \theta_L)$ of the left robot arm is $(40, 60, 30, -130)$, and the joint variable $(d_{R1}, d_{R2}, d_{R3}, \theta_R)$ of the right robot arm is $(80, 20, 10, 30)$;
- (4) The inverse kinematics solution results in the joint variable being equal to the initial assignment, which proves that the kinematics model is correct.

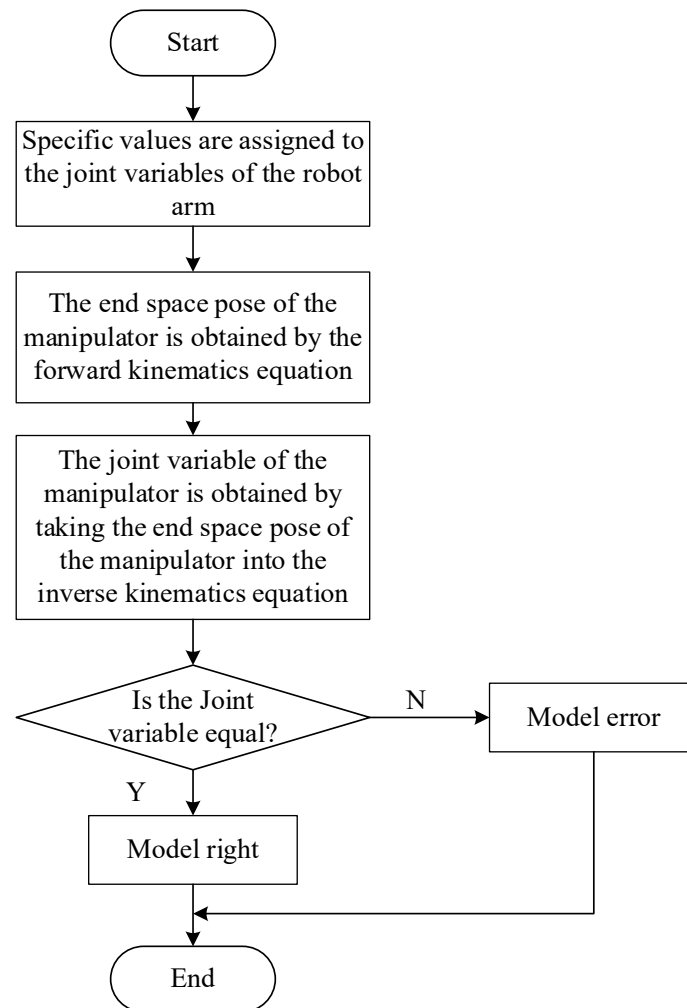


Figure 27. Kinematics simulation process.

4.3.2. Joint Kinematics Simulation of the Cabin Docking Robot and Cabin Workpiece

(1) Simulation parameter setting

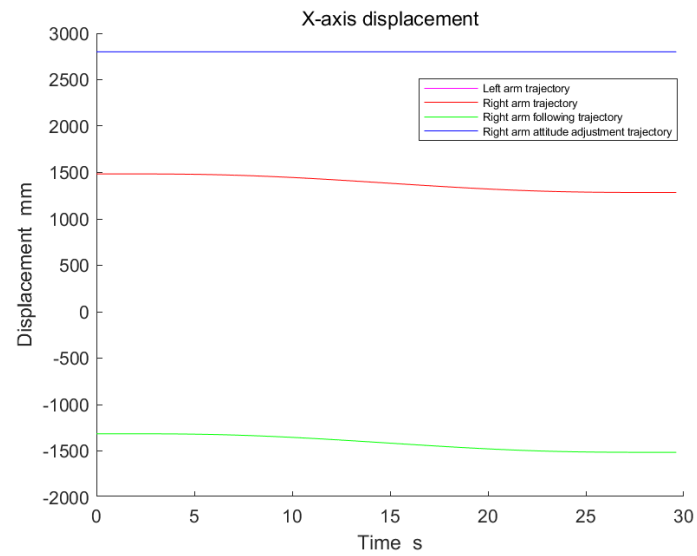
The pose starting and ending points of the simulation process are

$$\begin{cases} p_o = [-1315, -35, 775, 0.2, -0.2, 190] \\ p_e = [-1515, -5, 745, 0, 0, 180] \end{cases} \quad (14)$$

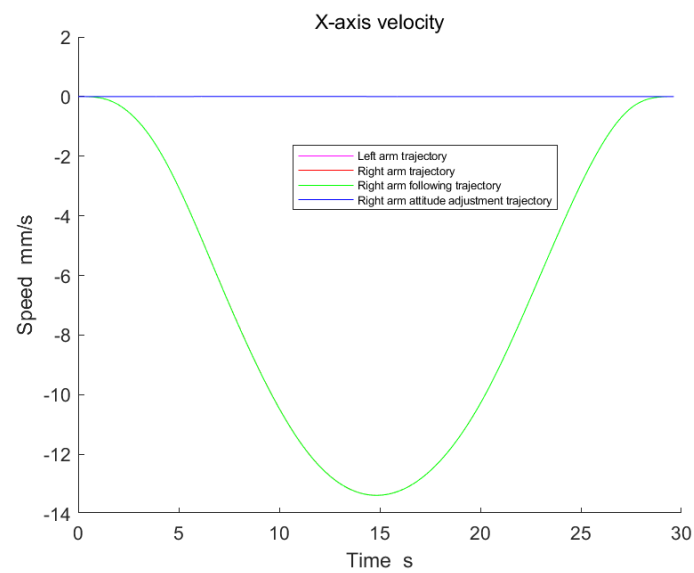
The elements in the vector represent, from left to right, the X-axis position, Y-axis position, Z-axis position, pitch angle, yaw angle, and rolling angle of the cabin workpiece.

(2) Results of joint kinematics simulation

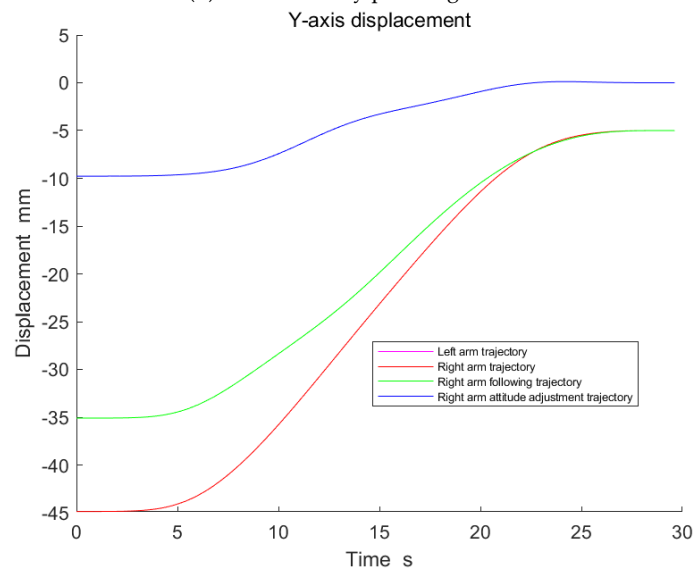
In order to verify the effectiveness of the joint kinematics modeling of the module docking robot and the module workpiece, the B-spline curve is used to plan the motion trajectory of the robot arm. The simulation results are shown in Figure 28.



(a) X-axis displacement planning curve

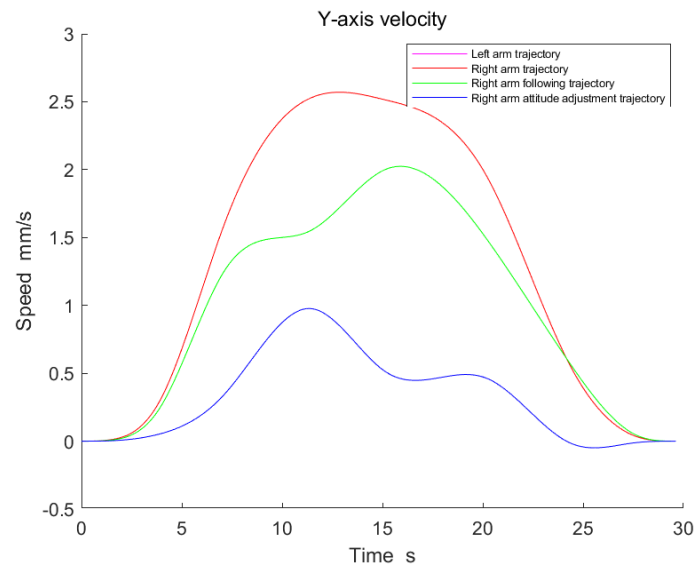


(b) X-axis velocity planning curve

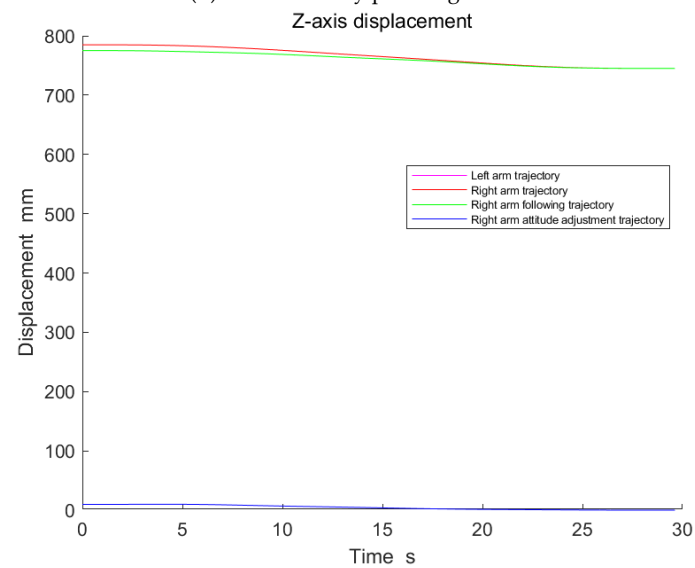


(c) Y-axis displacement planning curve

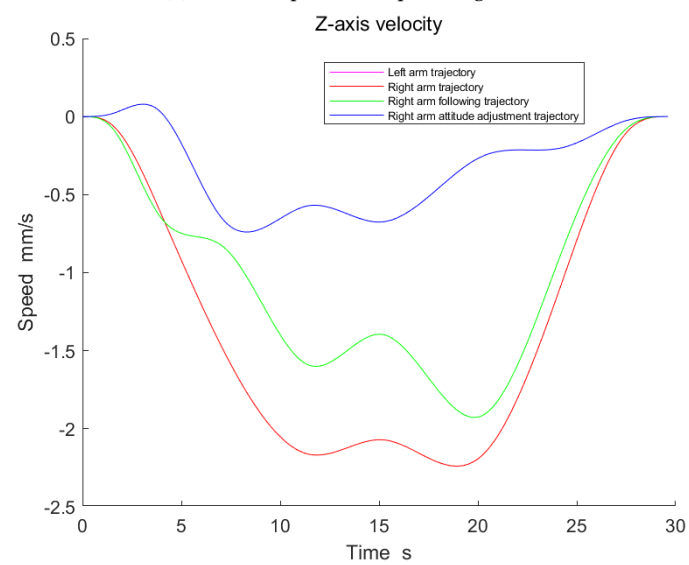
Figure 28. Cont.



(d) Y-axis velocity planning curve



(e) Z-axis displacement planning curve



(f) Z-axis velocity planning curve

Figure 28. Results of the joint kinematic trajectory simulation.

It is assumed that the right robotic arm trajectory consists of the following two parts: the following trajectory of the right robotic arm and the attitude adjustment trajectory of the right robotic arm. As can be seen in Figure 28, when the left robotic arm runs from the starting position p_o to the stopping position p_e , the planned displacement and planned speed of the left robotic arm are stable in the X-, Y-, and Z-axis directions. At the same time, the following trajectory of the right robotic arm and the trajectory of the left robotic arm coincide, and the running trajectory of the right robotic arm is equal to the synthesis of the following trajectory of the right robotic arm and the attitude adjustment trajectory of the right robotic arm. This verifies the effectiveness of the joint kinematic modeling of the docking arms in the cabin.

5. Experimental Verification

5.1. Development of a Prototype Robot System for Cabin Docking

The experimental platform of the cabin docking robot system is composed of a fixed cabin, a moving cabin, a fixed bracket, and the docking robot. The fixed cabin is placed on the fixed bracket, and the relative posture remains unchanged. The space pose adjustment of the moving cabin is realized by the docking robot. Finally, the docking between the mobile module and the fixed module is completed. The experimental platform of the cabin docking robot system is shown in Figure 29.



Figure 29. Experimental platform of the cabin docking robot system.

In Figure 29, the main specifications of the motor, encoder, driver and motion control system of the experimental platform are shown in Table 4.

Table 4. Main selection parameters of servo motor and reducer.

Name	Specification Parameter	Brand
Motor	EX310ESPB1511	Parker
Driver	C3S015V4F10I31T11M00	Parker
X-axis reducer	ABR060 L2-40-P2-S2	Newstart
Y-axis reducer	ABR060 L2-20-P1-S2	Newstart
Z-axis reducer	ABR060 L1-10-P2-S2	Newstart
Controller	CX5140-0135	Beckhoff
Digital output module	EL2809	Beckhoff
Digital input module	EL1808	Beckhoff
Analog input module	EXL3152	Beckhoff
Power module	EXL9560	Beckhoff

5.2. Workspace Test Experiment

5.2.1. Experimental Methods

The work space test experiments were carried out for the axial moving joint, radial moving joint, vertical lifting moving joint, and circular rotating joint of the cabin docking robot, and the experimental results were recorded for analysis.

The test method of working space of moving joint is as follows: set the starting position of the moving joint as D_0 (mm), move forward to the limit position, and record the value as D_{i+} (mm). Move to the limit position in the reverse direction, record the value as D_{i-} (mm), calculate the range of motion $D_i = (D_{i+} - D_{i-})$, and determine whether the range of movement covers the design index.

The test method of repeated positioning accuracy of rotational joint is as follows: set the starting position of the rotational joint as A_0 ($^{\circ}$), move forward to the limit position, and record the value as A_{i+} ($^{\circ}$). Move to the limit position in the reverse direction, record the value as A_{i-} ($^{\circ}$), calculate the angle range $A_i = (A_{i+} - A_{i-})$, and determine whether the motion range of the rotational joint covers the design index.

5.2.2. Experimental Results

The working space test results of the axial movement joint, the vertical lifting joint, and the radial movement joint are shown in Table 5. The working space test result of the circular rolling joint is shown in Table 6.

Table 5. Range of motion of the moving joint.

Joint Name	D_{i+} (mm)	D_{i-} (mm)	Displacement (mm)
Axial movement joint	3150	−13	3163
Vertical lifting joint	55	−46	101
Radial movement joint	−1	−102	101

Table 6. Range of motion of the rotational joint.

Joint Name	A_{i+} ($^{\circ}$)	A_{i-} ($^{\circ}$)	Angle ($^{\circ}$)
Circular rotating joint	10.1	−10.2	20.3

As can be seen in Tables 5 and 6, the motion displacement of the axial moving joint is 3163 mm, the motion displacement of the vertical lifting joint is 101 mm, the motion displacement of the radial moving joint is 101 mm, and that of the circular rolling joint is 20.3° . All of these values meet the design index requirements in Table 1.

5.3. Repeated Joint Positioning Accuracy Test

5.3.1. Experimental Methods

Repeated positioning accuracy tests were carried out for the axial moving joint, the radial moving joint, the vertical lifting joint, and the circular rotating joint, and the experimental results were recorded for analysis.

The test method of repeated positioning accuracy of moving joint is as follows: select an initial position on a movable joint and fix the dial indicator. Offset a distance L_0 (mm) and then return to the initial position and read the dial indicator value. The repeated positioning accuracy of each joint was obtained by statistical standard deviation of dial indicator values.

The test method of repeated positioning accuracy of rotational joint is as follows: install and fix the dial indicator at 400 mm of the center of circular rotating joint arc rolling body. Rotate a fixed angle A_0 ($^{\circ}$) and then return to the initial position and read the dial indicator value. The repeated positioning accuracy of each joint was obtained by the statistical standard deviation of dial indicator values.

5.3.2. Experimental Results

The repeated positioning accuracy test results of the axial moving joint, the radial moving joint, the vertical lifting joint, and the circular rotating joint are shown in Table 7, Table 8, Table 9, and Table 10, respectively.

Table 7. Experimental results of repeated positioning accuracy of the axial movement joint.

Number	10 mm	30 mm	50 mm	70 mm	90 mm
1	2.879	2.85	2.81	2.82	2.83
2	2.86	2.83	2.81	2.83	2.83
3	2.87	2.85	2.83	2.82	2.84
Standard deviation	0.009504	0.011547	0.011547	0.005774	0.005774

Table 8. Experimental results of repeated positioning accuracy of the radial movement joint.

Number	5 mm	10 mm	15 mm	20 mm	25 mm
1	2.75	2.74	2.73	2.73	2.73
2	2.74	2.73	2.73	2.73	2.73
3	2.74	2.73	2.73	2.73	2.73
Standard deviation	0.005774	0.005774	0	0	0

Table 9. Experimental results of repeated positioning accuracy of the vertical lifting joint.

Number	5 mm	10 mm	15 mm	20 mm	25 mm
1	2.73	2.75	2.76	2.75	2.76
2	2.74	2.75	2.75	2.75	2.76
3	2.74	2.75	2.76	2.75	2.76
Standard deviation	0.005774	0	0.005774	0	0

Table 10. Experimental results of repeated positioning accuracy of the circular rotary joint.

Number	0.5°	1°	1.5°	2°	2.5°
1	2.46	2.54	2.61	2.63	2.63
2	2.46	2.54	2.62	2.63	2.63
3	2.46	2.54	2.62	2.63	2.62
Standard deviation	0	0	0.005773503	0	0.005773503

As listed in Tables 7–10, the maximum and minimum standard deviation of the measurement values of the axial mobile joint repeated positioning are 0.011547 mm and 0.005774 mm, respectively. The maximum and minimum standard deviations of the repeated positioning measurements of the radial shifting joint and the vertical lifting joint are 0.005774 and 0 mm, respectively. The maximum and minimum standard deviation of the repeated positioning measurement values are 0.005774 mm and 0 mm, respectively.

According to the above test results, the maximum standard deviation of the repeated positioning accuracy measurement value of each joint of the cabin docking robot is 0.011547 mm, which meets the design requirements.

5.4. Precision Experiment of Joint Motion Control

In order to test the precision of joint motion control and set the target moving displacement value of the joint, the actual moving displacement value of the joint was obtained with the joint positioning control experiment through the MC_MoveAbsolute function block of the controller. The displacement error of the joint motion was obtained through calculation, and whether the displacement error of the joint motion was within the allowable range was determined.

5.4.1. Control Accuracy of the Axial Movement Joint

The axial movement joint is controlled to move the fixed displacement of 40 mm. The displacement change curve in the moving process is collected, and the displacement control accuracy is calculated. The collected displacement curve is shown in Figure 30.

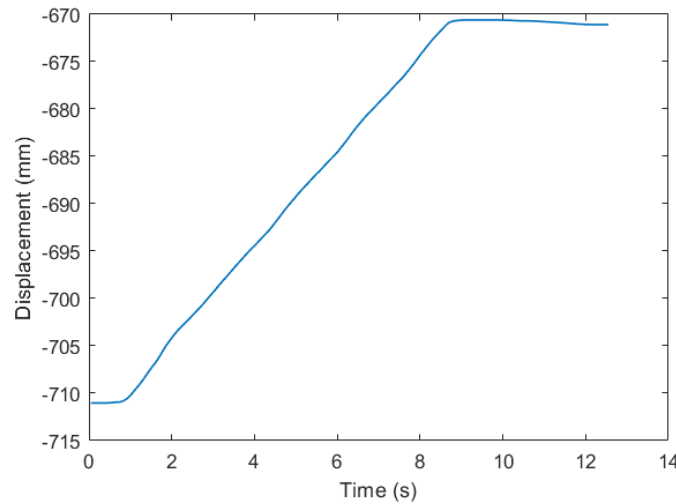


Figure 30. Displacement curve of 40 mm axial movement.

It can be seen in Figure 30 that when the axial moving joint moves 40 mm, the displacement motion is stable. The starting position of the joint movement is -711.027 mm, the target value of the stopping position of the joint movement is -671.027 mm, and the actual value of the stopping position of the joint movement is -671.085 mm. The motion error of the stopping position of the axial moving joint is 0.058 mm.

5.4.2. Control Accuracy of Vertical Lifting Joint

The vertical lifting joint was controlled to drop 5 mm. The displacement curve in the moving process was collected, and the displacement control accuracy was calculated. The collected displacement curve is shown in Figure 31.

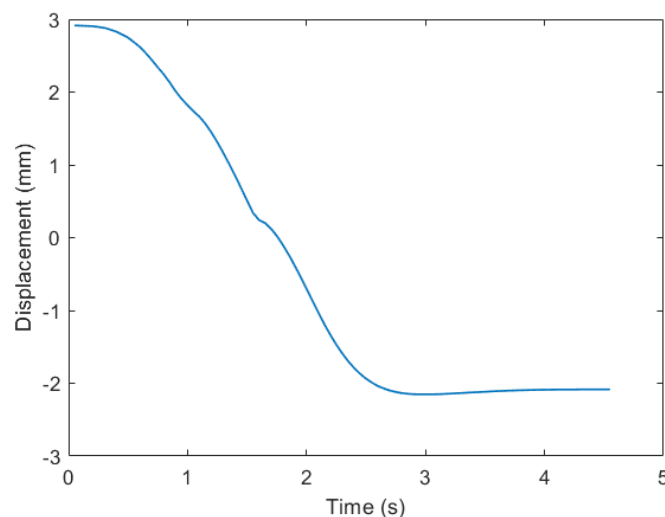


Figure 31. Displacement curve of vertical descent of 5 mm.

It can be seen in Figure 31 that when the vertical lifting joint moves 5 mm, the displacement movement process is stable. The starting position of joint motion is 2.914 mm, the target value of joint motion stop position is -2.086 mm, and the actual value of joint

motion stop position is -2.085 mm. The motion error of vertical lifting joint stop position is 0.001 mm.

5.4.3. Control Accuracy of the Radial Movement Joint

The radial mobile joint was controlled to move the fixed displacement 10 mm. The displacement change curve in the moving process was collected, and the displacement control accuracy was calculated. The collected displacement curve is shown in Figure 32.

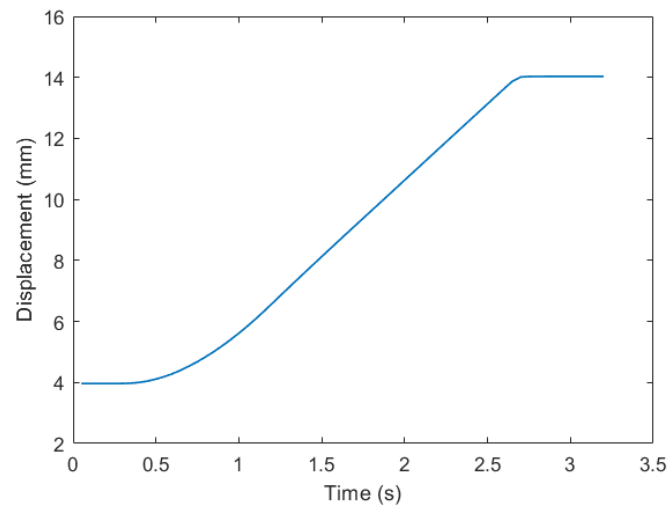


Figure 32. Displacement curve of radial movement of 10 mm.

It can be seen in Figure 32 that when the radial mobile joint moves 10 mm, the motion of displacement and velocity is stable. The initial position of the joint motion is 3.966 mm, the target value of the joint motion stop position is 13.966 mm, and the actual value of the joint motion stop position is 14.031 mm. The motion error of the radial moving joint stop position is 0.0065 mm.

5.4.4. Control Accuracy of the Circular Rolling Joint

The circular rolling joint was controlled to fix the angle of circular rolling 2° . The change curve of the angle in the moving process was collected, and the angle control accuracy was calculated. The collected angle curve is shown in Figure 33.

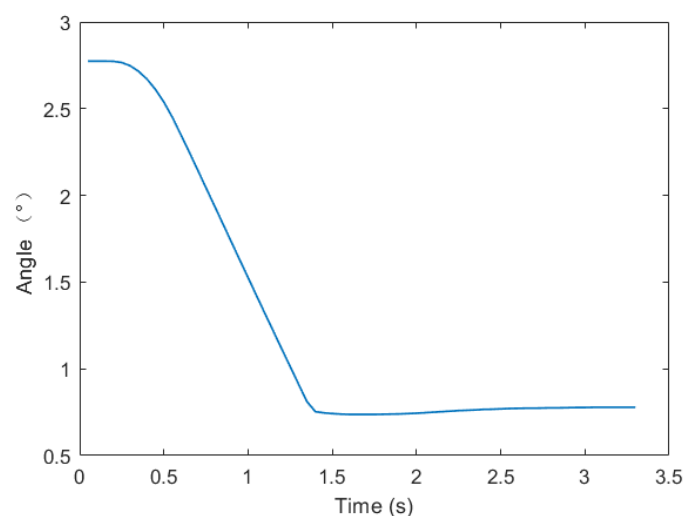


Figure 33. Angular curve of the 2° circular roll.

As can be seen in Figure 33, when the circular rolling joint is rotated by 2° , the angular motion process is stable. The initial angle of joint motion is 2.774° , the target value of joint motion stopping angle is 0.774° , and the actual value of joint motion stopping position is 0.778° . The motion error of radial moving joint stopping position is 0.004° .

5.5. Cabin Docking Experiment

According to the working principle of the cabin docking robot system, the control system block diagram of the cabin docking robot is designed, as shown in Figure 34.

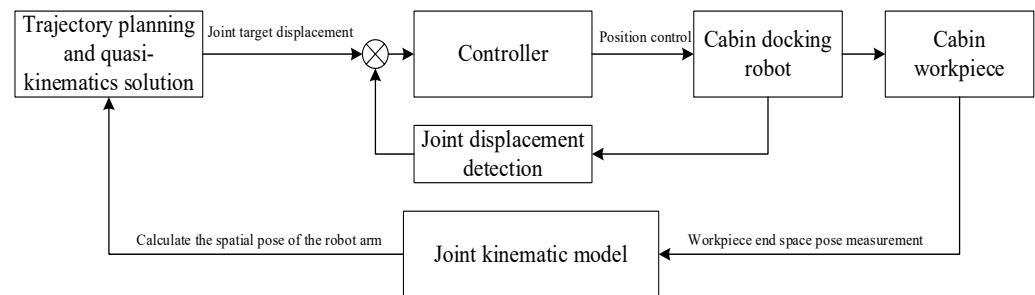


Figure 34. Block diagram of the docking control system of the docking robot.

In Figure 34, an external laser tracker is used to measure the six characteristic quantities of the workpiece end face center coordinate $O_1(x_1, y_1, z_1)$, pitch angle α , yaw angle β , and rolling angle γ and convert them into the end coordinate $O_L(x_L, y_L, z_L)$ of the docking robot arm by Equation (13). Then, the target displacement of each joint is calculated through trajectory planning and inverse kinematics. Finally, the MC_MoveAbsolute function block of the servo drive is invoked to control the position of the joint.

In the process of cabin docking, the starting position of the module docking robot in the Z-axis direction is 100 mm, and the stopping position is set to -1.99 mm. The planned target trajectory is compared with the actual trajectory collected, as shown in Figure 35.

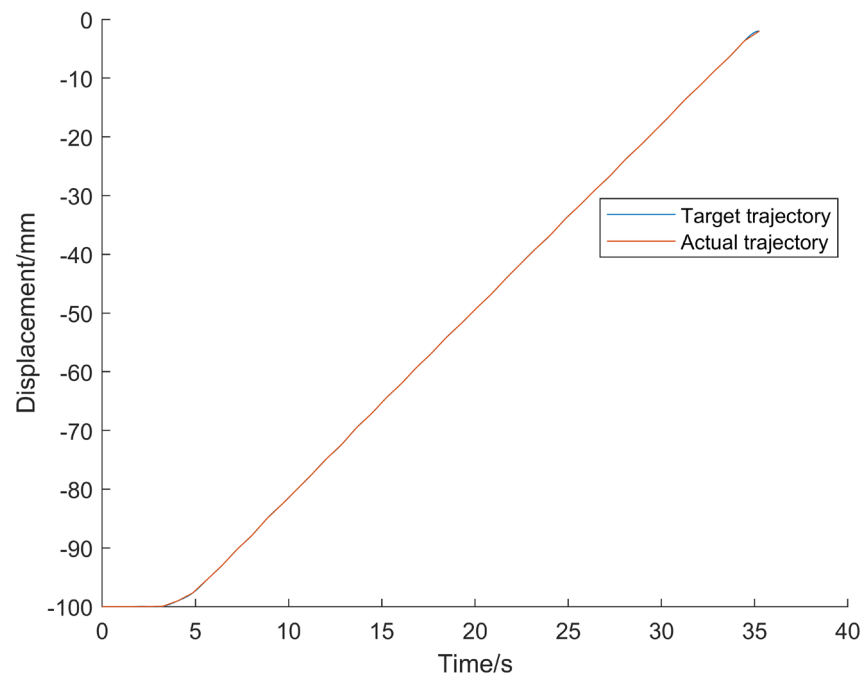


Figure 35. Trajectory control curve of the cabin docking robot in the Z-axis direction.

In Figure 35, the maximum displacement error between the target trajectory and the actual trajectory is 0.377 mm and the minimum error is 0 mm.

In the process of cabin docking, the start position of the cabin docking robot in the Y-axis direction is 30 mm, and the stop position is set to 0.63 mm. The planned target trajectory is compared with the actual trajectory collected, as shown in Figure 36.

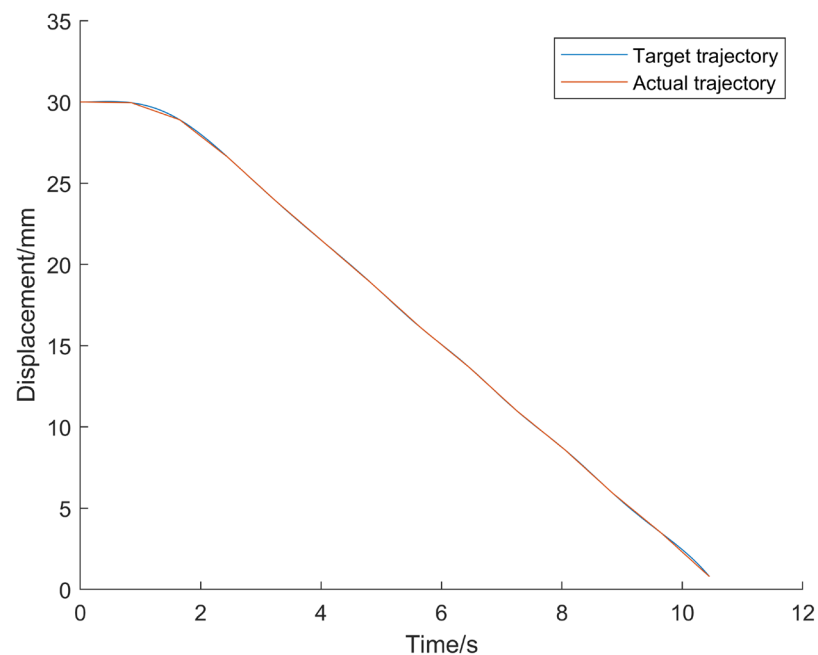


Figure 36. Trajectory control curve of the cabin docking robot in the Y-axis direction.

In Figure 36, the maximum displacement error between the target trajectory and the actual trajectory is 0.4655 mm and the minimum error is 3.333×10^{-5} mm.

5.6. Comparison of Robot Performance Indicators

In order to evaluate the performance advancement of the cabin docking robot system, the performance indicators of the module docking robot are compared with those of the standard heavy-load industrial robot (KR 1000 L950 TITAN PA). The comparison results are shown in Table 11.

Table 11. Comparison table of robot specification parameters.

Name	Cabin Docking Robot	Standard Industrial Robot	Comparison Result
Load	Max. 1000 kg	1000 kg	Same level
Degree of freedom	6	6	Same level
Repeated positioning accuracy	± 0.05 mm	± 0.2 mm	Higher level
Installation position	Ground	Ground	Same level
Work space	Circumference: $\pm 15^\circ$; Axis: ± 600 mm; Vertical: ± 50 mm; Radial: ± 50 mm;	Max. 3601 mm	Lower level

It can be seen from Table 11 that compared with standard industrial robots, the cabin docking robot is at the same level in terms of load, freedom, and installation position indicators. In terms of repeated positioning accuracy, the cabin docking robot is superior to the standard industrial robot. But in terms of scope of work, the cabin docking robot is lower than standard industrial robots.

6. Conclusions

In this paper, a cabin docking robot system is designed, the strength and kinematics of the key mechanical components of the robot are analyzed, and the key indexes of the robot system are verified by a prototype.

- (1) The cabin docking robot is designed by the horizontal docking mode, and the composition and working principle of each joint of the robot are analyzed. The degree of freedom of the cabin docking robot is six, and the maximum load capacity can reach 1000 kg.
- (2) The static stress analysis of the key components of the robot joints is carried out by finite element software. The maximum equivalent stress of the bottom frame is 31.81 Mpa and the maximum total deformation is 0.125 mm. The maximum equivalent stress of the trapezoidal lead screw is 28.86 Mpa, and the maximum total deformation is 0.0177 mm. The maximum equivalent stress of the shell bracket is 23.13 Mpa, and the maximum total deformation is 0.0182 mm. The maximum equivalent stress of the rolling bearing is 9.153 Mpa, and the maximum total deformation is 0.001195 mm. The simulation results are all within the reasonable range.
- (3) The kinematics model of the robot is established based on the D-H modeling method, the forward and inverse kinematics relationship of the robot are analyzed, and the correctness of the kinematics model of the robot is verified by simulation.
- (4) The cabin docking robot and the joint kinematics model of the module are established and the correctness of the joint kinematics model is verified through simulation.
- (5) The working space, repeated positioning accuracy, and motion control accuracy of each joint of the robot are verified through experiments, which proved the effectiveness of the robot design.

Based on the above analysis, the cabin docking robot system designed in this paper can meet the automatic attitude adjustment function of medium and large module workpieces. It has the advantages of a strong bearing capacity, a simple control algorithm, high stiffness, decoupling of degrees of freedom, and so on. However, the total structure of the module docking robot is large, and the area is also large, which brings certain restrictions to the field application.

In addition, it is necessary to strengthen the speed control algorithm in subsequent research.

Author Contributions: Conceptualization, R.L. and F.P.; methodology, R.L.; software, R.L.; validation, R.L.; formal analysis, R.L.; investigation, R.L.; resources, R.L.; data curation, R.L.; writing—original draft preparation, R.L.; writing—review and editing, F.P.; visualization, F.P.; supervision, F.P.; project administration, F.P.; funding acquisition, F.P. All authors have read and agreed to the published version of the manuscript.

Funding: We would like to express our gratitude to the National Natural Science Foundation of China (No. 61973036), the National Natural Science Foundation of China (No. 62261160575), and the National Natural Science Foundation of China (No. 61991414).

Data Availability Statement: The original contributions presented in the study are included in the article material, further inquiries can be directed to the corresponding author.

Conflicts of Interest: The authors declare no conflict of interest.

References

1. Guo, Z.M.; Jiang, J.X.; Ke, Y.L. Posture Alignment for Large Aircraft Parts Based on Three POGO Sticks Distributed Support. *Acta Aeronaut. Astronaut. Sin.* **2009**, *30*, 1319–1324.
2. Guo, Z.M.; Jiang, J.X.; Ke, Y.L. Design and accuracy for POGO stick with three-axis. *J. Zhejiang Univ. (Eng. Sci.)* **2009**, *43*, 1649–1654.
3. Jiang, J.X.; Chen, Q.; Fang, Q.; Ke, Y. Analysis and experimental test on dynamic characteristic of 3-axis positioner system. *Comput. Integr. Manuf. Syst.* **2009**, *19*, 1004–1009.

4. Zhang, B.; Yao, B.; Ke, Y. A novel posture alignment system for aircraft wing assembly. *J. Zhejiang Univ. Sci. A* **2009**, *10*, 1624–1630. [\[CrossRef\]](#)
5. Yuan, X.; Tang, Y.; Wang, W.; Zhang, L. Parametric Vibration Analysis of a Six-Degree-of-Freedom Electro-Hydraulic Stewart Platform. *Shock. Vib.* **2021**, *2021*, 1–27. [\[CrossRef\]](#)
6. Jin, H.R.; Liu, D. Two-point Positioning and Pose Adjustment Method for Automatic Assembly of Barrel-type Cabin. *China Mech. Eng.* **2018**, *29*, 1467–1474.
7. Dai, W.B.; Hu, R.Q.; Yi, W.M. The flexible docking technology for large spacecraft cabins. *Spacecr. Environ. Eng.* **2014**, *31*, 584–588. [\[CrossRef\]](#)
8. Xiong, T. Automatic Docking Technology of Satellite. *Aeronaut. Manuf. Technol.* **2011**, *22*, 36–39. [\[CrossRef\]](#)
9. Wang, B.X.; Xu, Z.G.; Wang, J.Y.; Wang, Y.J. Design and Research of Missile General Assembly Automatic Docking Platform. *Mod. Def. Technol.* **2016**, *44*, 135–141+147.
10. Yi, W.M.; Duan, B.W.; Gao, F.; Han, X.G. Level docking technology in large cabin assembly. *Comput. Integr. Manuf. Syst.* **2015**, *21*, 2354–2360. [\[CrossRef\]](#)
11. Guo, J.; Zhang, X.; Li, H.; Sun, X. Mechanism Design and Strength Analysis of Key Components of Flight-climbing-slide Robot for High-voltage Transmission Line Inspection. In Proceedings of the 2017 IEEE 7th Annual International Conference on CYBER Technology in Automation, Control, and Intelligent Systems (CYBER), Honolulu, HI, USA, 1 July–4 August 2017.
12. Pao, J.C.; Banglos, C.A.; Salaan, C.J.; Guirnaldo, S.A. Simulation and Strength Analysis of Flippable Mobile Ground Robot for Volcano Exploration and Monitoring Application. In Proceedings of the 2022 IEEE 14th International Conference on Humanoid, Nanotechnology, Information Technology, Communication and Control, Environment, and Management (HNICEM), Boracay Island, Philippines, 1–4 December 2022.
13. Xu, M.; Zhang, Z.; Shao, L.; Zhang, Z.; Cao, C. Analysis and Calculation of Strength and Rigidity for Industrial Grinding Robot. In Proceedings of the 2022 12th International Conference on CYBER Technology in Automation, Control, and Intelligent Systems (CYBER), Baishan, China, 27–31 July 2022.
14. Denavit, J.; Hartenberg, R. A kinematic notation for lower-pair mechanisms based on matrices. *J. Appl. Mech.* **1955**, *22*, 215–221. [\[CrossRef\]](#)
15. Hayati, S.; Mirmirani, M. Improving the absolute positioning accuracy of robot manipulators. *J. Robot. Syst.* **1985**, *2*, 397–413. [\[CrossRef\]](#)
16. Ajayi, O.K.; Arojo, T.A.; Ogunnaike, A.S.; Adeyi, A.J.; Olanrele, O.O. Performance Enhancement with Denavit-Hartenberg (D-H) Algorithm and Faster-RCNN for a 5 DOF Sorting Robot. In *Mechatronics and Automation Technology, Proceedings of the 2nd International Conference (ICMAT 2023), Wuhan, China, 28–29 October 2023*; IOS Press: Amsterdam, The Netherlands, 2024; pp. 459–466.
17. Xiao, P.; Ju, H.; Li, Q.; Meng, J.; Chen, F. A new fixed axis-invariant based calibration approach to improve absolute positioning accuracy of manipulators. *IEEE Access* **2020**, *8*, 134224–134232. [\[CrossRef\]](#)
18. Zhu, Z.; Ma, G.; Liu, H.; Liu, B. D-H model and continuous trajectory planning for orbital welding robot of box-type steel structure. *Hanjie Xuebao/Trans. China Weld. Inst.* **2017**, *38*, 95–98.
19. Li, X.; Wang, H.; Lu, X.; Liu, Y.; Chen, Z.; Li, M. Neural network method for robot arm of service robot based on DH model. In Proceedings of the 2017 Chinese Automation Congress (CAC), Jinan, China, 20–22 October 2017.
20. Pan, Y.; Lu, Y.; Liu, C. Research on welding trajectory planning of MOTOMAN-MA1440 robot based on MATLAB robotics toolbox. In Proceedings of the Third International Conference on Control and Intelligent Robotics (ICCIR 2023), Changsha, China, 23–25 May 2023; Volume 12940.
21. Aliakbari, M.; Mahboubkhah, M.; Sadaghian, M.; Barari, A.; Akhbari, S. Computer integrated work-space quality improvement of the C4 parallel robot CMM based on kinematic error model for using in intelligent measuring. *Int. J. Comput. Integr. Manuf.* **2022**, *35*, 444–461. [\[CrossRef\]](#)
22. Li, X.P.; Yang, Y.; Tian, G.Q.; Li, S.Q.; Wang, J.Y. Life Calculation and Reliability Analysis of Turbine Wheel Based on Monte Carlo Method. *J. Chin. Soc. Power Eng.* **2023**, *43*, 1434–1439+1530.
23. Zhang, F.; Yu, G.; He, S.; He, W. An-improved α -Shapes algorithm for solving collaborative workspaces of dual SCARA robots based on Monte Carlo method. In Proceedings of the 2023 42nd Chinese Control Conference (CCC), Tianjin, China, 24–26 July 2023; Volume 5. [\[CrossRef\]](#)
24. Tomáš, S.; Jozef, S.; Štefan, O. Mapping Robot Singularities through the Monte Carlo Method. *Appl. Sci.* **2022**, *12*, 8330.
25. Gao, H.; Xu, Y. The solution of the volume of collaborative space of 6R two-arm robot based on the body-elemental algorithm. *Acad. J. Eng. Technol. Sci.* **2022**, *5*, 60–67.

Disclaimer/Publisher’s Note: The statements, opinions and data contained in all publications are solely those of the individual author(s) and contributor(s) and not of MDPI and/or the editor(s). MDPI and/or the editor(s) disclaim responsibility for any injury to people or property resulting from any ideas, methods, instructions or products referred to in the content.